JOURNAL OF GEOPHYSICAL RESEARCH, VOL. 106, NO. A7, PAGES 12,933–12,952, JULY 1, 2001

A self-consistent model of the Jovian auroral thermal structure

Denis Grodent

LPAP, Institut d'Astrophysique et de Géophysique, Université de Liège, Belgium

J. Hunter Waite Jr.

Southwest Research Institute, San Antonio, Texas

Jean-Claude Gérard

LPAP, Institut d'Astrophysique et de Géophysique, Université de Liège, Belgium

Abstract. A one-dimensional (1-D) model coupling a two-stream electron transport model of energy deposition with a 1-D thermal conduction model has been developed. It is applied to investigate the links between auroral heat input and the vertical temperature of Jupiter's upper atmosphere. Two energy distributions meant to reproduce the emissions of a diffuse and a discrete aurora are used to evaluate the importance of the energy spectrum of the incident electrons for the thermal balance of Jupiter's auroral thermosphere. The values of observable quantities such as the altitude of the H_2 emission peak, thermal infrared (IR), ultraviolet (UV) emissions, and temperatures associated with various optical signatures are used to constrain the parameters of these distributions. It is shown that the high-energy component of these energy distributions heats a region of the homosphere between 10^{-4} and 10^{-6} bar and mainly controls the H_2 temperature and the far-UV (FUV) emission. A 3-keV soft electron component is necessary to heat the region directly above the homopause, between 10^{-6} and 10^{-9} bar. It has a large influence on the H_2 and H_3^+ temperatures and on the H_3^+ near-IR (NIR) emission. It is used in conjunction with a weak 100 eV component which is responsible for heating the thermosphere, from 10^{-9} to 10^{-12} bar and exerts a control on the exospheric temperature. The calculated temperatures, UV, and IR emissions suggest that the model probably misses a nonparticle heat source in the 10^{-5} bar region, that is expected to balance the strong hydrocarbon cooling. Sensitivity tests are performed to evaluate the importance of the parameters of the energy distributions. They show that the FUV color ratio increases with the characteristic energy (or high-energy cutoff) of the high-energy component, while the H_2 rovibrational temperature varies inversely. A trade-off is therefore necessary for these two parameters to simultaneously meet their observational constraints. Further tests demonstrate the essential thermostatic role played by H_3^+, which regulates the net heating in the thermosphere. An increased eddy diffusion reproduces the effect of a possible auroral upwelling of methane but gives rise to an H_2 temperature smaller than the observed value.

1. Introduction

Recent progress in imaging and spectroscopy of the Jovian aurora have considerably increased and improved our knowledge of the energetics induced by particle input and its potential effect on the thermospheric thermal structure of the planet. Spectroscopic observations of the UV aurora with the International Ultraviolet Explorer (IUE) satellite [*Livengood et al.*, 1990] and the ultraviolet spectrometer (UVS) onboard the Voyager spacecraft [*Broadfoot et al.*, 1979] suggest a total auroral particle input flux of the order of 10^{13}-10^{14} W in each hemisphere, about 3 orders of magnitude stronger than the corresponding value for the Earth's aurora. Such a large energy flux has been confirmed by UV images of the Jovian aurora obtained with the Faint Object Camera (FOC) [*Gérard et al.*, 1993, 1994] and the Wide Field Planetary Camera (WFPC2) [*Clarke et al.*, 1998; *Morrisey et al.*, 1997] on board the Hubble Space Telescope (HST). The large amount of energy input into the atmosphere (~100 times the global extreme ultraviolet (EUV) solar energy input) produces ionization, radiation, and particle heating in the planet's upper atmosphere. Since the energy flux in the auroral regions is so much larger than the solar heating in the thermosphere, it is expected that the auroral processes maintain the large exospheric temperature observed at midlatitude and high latitude.

One-dimensional models of the interaction between energetic primary particles and the Jovian atmosphere have been previously developed. These models used the continuous slowdown approximation for electrons [*Heaps et al.*, 1973; *Gérard and Singh*, 1982], the two-stream approximation for electrons [*Waite et al.*, 1983], protons [*Rego et al.*, 1994], and energetic oxygen auroras [*Horanyi et al.*, 1988]. *Kim et al.* [1992] and more recently, *Perry et al.* [1999] applied a multistream electron transport code to predict the ion chemistry induced by the precipitation of monoenergetic electrons in the Jovian auroral

Paper number 2000JA900129.
0148-0227/01/2000JA900129$09.00

atmosphere. Most of these studies assumed that the energy input is carried by electrons rather than protons or heavy ions [*Waite et al.*, 1994]. This assumption is justified by the lack of evidence for strong proton precipitation in the Lyman α line profile [*Clarke et al.*, 1994] and the absence of characteristic lines expected for O^+ and S^+ ion precipitation [*Trafton et al.*, 1998; *Liu et al.*, 2000]. Furthermore, model studies indicate that about 50% of the electron beam energy is ultimately converted into heating of the neutral atmosphere [*Gérard and Singh*, 1982; *Waite et al.*, 1983, 1997]. However, in these studies the thermal vertical structure and the atmospheric composition were prescribed, based on data collected by UV occultation or by the Galileo probe in the equatorial regions.

Information on the thermospheric thermal structure has three principal sources covering different altitude regions: (1) hydrocarbon infrared measurements at pressures around 10^{-4} to 10^{-6} bar, (2) H_2 rovibrational temperatures derived from ultraviolet spectra in the 10^{-5} to 10^{-8} bar range, and (3) H_3^+ spectra in the 10^{-6} to 10^{-10} bar pressure range. A reanalysis of the temperature structure in the north auroral region was performed by *Drossart et al.* [1993a] using the Voyager 1 infrared interferometer and radiometer spectrometer (IRIS) data. The infrared (IR) excess emission rate by the hydrocarbons was found to be ~93 ergs cm^{-2} s^{-1} by methane and ~86 ergs cm^{-2} s^{-1} by acetylene averaged over an auroral hot spot. Good agreement with the data was obtained by adopting a steep temperature gradient near the homopause reaching lapse rate values of about 2 K/km. Rovibrational H_2 temperatures have been determined from observations of high-resolution (0.3-0.5 Å) UV spectra obtained with the Goddard High Resolution Spectrograph (GHRS) on board HST [*Clarke et al.*, 1994; *Trafton et al.*, 1994, 1998; Liu and Dalgarno, 1996; *Kim et al.*, 1997; *Dols et al.*, 2000]. The H_2 temperature reflects the temperature along the line of sight weighted by the auroral volume emission rate. It was found to vary between 300 and 700 K with little correlation to the H_2 emission brightness. Additional information on the thermospheric auroral temperature is provided by the analysis of the rovibrational structure of the H_3^+ fundamental band near 3.5 μm [*Trafton et al.*, 1989; *Drossart et al.*, 1989; *Miller et al.*, 1990; *Lam et al.*, 1997]. These measurements indicate that the H_3^+ temperature, which was shown to be close to the gas kinetic temperature [*Drossart et al.*, 1993b], varies between 700 and 1000 K (in addition a strong anticorrelation was found between the temperature and the H_3^+ column density). A neutral temperature structure constrained by these three sets of measurements, ranging from 200 K at 10^{-7} bar to 2100 K at 10^{-14} bar, was presented by *Trafton et al.* [1994].

No in situ measurement of Jupiter's auroral atmosphere vertical structure is available. The vertical profile derived from the Galileo probe [*Seiff et al.*, 1998] was obtained at a low-latitude site. The equilibrium exospheric temperature is controlled by the total particle energy input and the energy spectrum of the primary electrons. The H_3^+ concentration enhancements generated by the deposition of soft primary particles and secondary electrons act as an efficient cooling process for the thermosphere by transferring a large fraction of the energy input to the ionosphere and subsequently radiating most of it away into space. Another fraction of the heat input is conducted downward into the hydrocarbon layer where it radiatively cools to space through radiative stratospheric species, such as CH_4 and C_2H_2. The relative location of the heat source from auroral energy deposition and the altitude of the homopause (the level of the hydrocarbon onset) will determine, in a complex way, the relative importance of H_3^+ cooling, direct hydrocarbon radiation to space and downward conduction from the region of heat production to the hydrocarbon layer. The vertical distribution of hydrocarbons may also, in part, be controlled by the amount of heat dissipation below the homopause. Upwelling of hydrocarbon-rich gas due to the release of large amounts of auroral heat has been invoked as a possible source of hydrocarbon enhancement above a region of strong precipitation [*Livengood et al.*, 1990], similar to the N_2/O enhancement observed in the Earth's thermosphere during strong auroral disturbances. Inversely, a large auroral energy input near or below the homopause may cause a local temperature increase, resulting in a thermal expansion of the overlying atmosphere, a change of the altitude of the deposition peak and a resulting perturbation of the hydrocarbon cooling efficiency. This latter possibility is favored by recent visible-wavelength images obtained by the Galileo solid-state imaging (SSI) system [*Ingersoll et al.*, 1998] which places the altitude of the auroral nightside emission at 245 ±30 km above the 1 bar level [*Vasavada et al.*, 1999].

A one-dimensional model has been developed to address the question of the close coupling between auroral electron precipitation, and the atmospheric temperature and composition structure. It couples a two-stream electron transport model of energy deposition with a 1-D thermal conduction model including particle heating and CH_4, C_2H_2, and H_3^+ cooling [*Waite et al.*, 1997]. In the absence of in situ measurements of the energy distribution of the incident auroral electrons, two plausible distributions are used to investigate their influence on the thermal balance of Jupiter's auroral thermosphere. The values of observable quantities such as the altitude of the H_2 emission peak, IR and UV emissions and temperatures associated with various optical signatures are used to constrain the parameters of these distributions.

2. The Electron Energy Degradation Model

The energy degradation scheme used in the present model is an updated version of the model described by Waite *et al.* [1983]. A complete description of this new version of the model may be found in the work of *Grodent* [2000]. It is based on a two-stream electron transport method for the energetic electron flux in a planetary atmosphere, as described by *Nagy and Banks* [1970] and *Banks and Nagy* [1970]. A mean pitch angle is assumed for all transported electrons so that their distribution is approximated by an upward and a downward stream of electrons. The two-stream transport code calculates the flow and redistribution of the electron energy as a function of altitude from atomic and molecular processes by means of discrete energy bins. The use of a variable energy bin structure, with small 0.5 eV wide energy bins below 10 eV gradually increasing to 25-keV wide bins near 1 MeV, allows the treatment of complex energetic electron flux distributions spanning energies from 0.5 eV to 1 MeV. Once the electron fluxes are calculated, the rates of ionization, dissociation, heating, and emission processes can be determined. Auroral intensities from various spectral features are also calculated.

While traveling along magnetic field lines, the electrons undergo elastic and inelastic collisions with the major neutral constituents of the Jovian atmosphere H_2, H, and He. The elastic electron impact cross section is taken from *Moiseiwitsch* [1962] for He and from *Callaway* [1993] for H. The H_2 elastic cross section, the elastic backscatter probability, and the inelastic H_2 backscatter probability are derived from *Shyn and Sharp* [1980, 1981]. The elastic and inelastic backscatter probabilities for He

and H are assumed to be 0.5. Most of the inelastic electron impact cross sections are computed with the analytical formulation described by *Garvey et al.* [1977]. The B $^1\Sigma_u^+$ state, hereafter noted *B* (upper level of the H_2 Lyman band system) and the C $^1\Pi_u$ state, hereafter noted *C* (upper level of the H_2 Werner band system) are taken from *Liu et al.* [1998]. The *B'* $^1\Sigma_u^+$, *B''* $^1\Sigma_u^+$, D $^1\Pi_u$, and *D'* $^1\Pi_u$ H_2 Rydberg states (hereafter noted *B'*, *B"*, *D*, and *D'*, respectively) and the *E,F* Σ_g^+ (EF) excitation rates are computed with the analytical representation of *Shemansky et al.* [1985]. The $a^3\ \Sigma_g^+$ triplet state (*a*3) of H_2 cross section is compatible with *Ajello and Shemansky* [1993] and *Khakoo and Segura* [1994] and the $b^3\ \Sigma_u^+$ state (*b*3) excitation cross section is comparable with the measurements of *Rescigno et al.* [1993]. The $c^3\ \Pi_g$ (*c*3) excitation cross section is compatible with *Khakoo and Trajmar* [1986].

The Lyman α emission resulting from electron impact is produced by two mechanisms. The dominant mechanism is dissociative excitation of H_2. The cross section for this process is taken from *Ajello et al.* [1995]. The other source is direct excitation of H, with the cross section from *James et al.* [1997]. The Lyman β emission cross section from dissociative excitation of H_2 is from *Ajello et al.* [1996]. The differential ionization cross sections are computed following the formulation of *Green and Sawada* [1972], *Jackman et al.* [1977], and the relativistic formulation of *Garvey et al.* [1977]. They were scaled to match the total ionization cross sections measured by *Straub et al.* [1996] for H_2, *Bandyopadhyay et al.* [1995] for H, and *Stephan et al.* [1980] for He.

Rovibrational excitation by H_2 is a very efficient cooling process for low-energy electrons. The cross section for vibrational excitation of H_2 used is in agreement with *Buckman et al.* [1990] and *Miles et al.* [1972], and the rotational excitation cross section of H_2 has been fitted to the measurements of *Linder and Schmidt* [1971]. The analytical excitation cross sections described by *Ajello et al.* [1995] are adopted to account for doubly excited states of H_2. These states are responsible for the dissociation of H_2 in fast H(2*p*) and H(2*s*) fragments that are involved in the neutral heating process.

2.1. Heat Conservation Equation

To investigate the effects of the auroral electron precipitation on the thermal structure of the upper atmosphere, we consider the balance between heating, cooling, and transport of energy by thermal conduction [*Waite et al.*, 1997]. The neutral temperature profile is calculated according to the heat conduction equation

$$\frac{d}{dz}\left(\kappa\frac{dT}{dz}\right) = H_z - C_z \qquad \kappa = AT^s \tag{1}$$

where z is the altitude, T is the temperature, κ is the thermal conduction coefficient for H_2, with s=0.75 and A=252 ergs cm^{-2} s^{-1} K^{s+1} [*Hanley et al.*, 1970], and H_Z and C_Z are the local heating and cooling rates (in erg cm^{-3} s^{-1}), respectively. This differential equation is solved numerically with a two-point Gauss-Legendre quadrature method. The upper atmosphere boundary condition ensures the isothermicity of the exosphere and the lower boundary condition allows to impose a fixed stratospheric temperature at the bottom of the model.

2.2. Heat Sources

2.2.1. Assumed heat sources. The major electron heating mechanisms considered account for (1) the excess kinetic energy of the two fragments resulting from the electron impact dissociation of H_2; (2) the thermal electron cooling of the energetic electrons, and subsequent H_2 vibrational and rotational cooling of the thermal electrons; (3) the vibrational excitation of the ground electronic state of H_2 following Lyman and Werner band transitions; and (4) the chemical heating due to the formation of H_2^+ and H and subsequent reactions resulting in dissociative recombination of H_3^+ to produce H_2 and H. The energy stored into H^+ is not available for heating, since H^+ recombines radiatively unless charge exchange with H_2 ($v \geq 4$) occurs.

The average fractions of the transitions from the B state, including cascade from EF and from the *C* state terminating into the vibrational continuum of the ground state *X* $^1\Sigma_g^+$, (i.e., dissociation of H_2) are calculated from *Dalgarno and Stephens* [1970] and *Stephens and Dalgarno* [1972]. The average kinetic energy of the fragments is determined from *Stephens and Dalgarno* [1973] and is consistent within 5% with the temperature sensitive values given by *Abgrall et al.* [1997]. For the *B"*, *D* and *D'* excited states we used the branching ratios determined by *Ajello et al.* [1984] at 100 eV to discriminate the direct transitions to the ground state from the predissociation to the *B'* state. These branching ratios to the ground state are 3.3, 70.2, and 42.1%, respectively. The fraction of the transitions from the *D* excited state to the vibrational continuum of the ground state is from *Glass-Maujean et al.* [1984]. For the *B'* excited state we use *Kwok et al.* [1985] which is in agreement with *Liu and Dalgarno* [1996]. According to *Liu and Dalgarno* [1996], the *B"* and *D'* states, have approximately the same equilibrium separation as the *B'* and *D* states respectively. We thus consider the same fractions of transitions ending in the *X* $^1\Sigma_g^+$ continuum. Predissociation to B' and direct dissociation of singly excited states are considered in a global cross section determined by *Ajello et al.* [1995], giving rise to two "slow" H fragments carrying 0.3 eV each. The production of "fast" H(2*p*) fragments from dissociative excitation of a series of doubly excited states is also considered in the same reference. It is computed by combining two analytical cross sections giving mean fragments energies of 6.5 eV + 4 eV(40%) and 2 times 4 eV(60%), respectively. In order to account for the energy carried by the H(2*s*) fragments we have considered that the singly excited states give rise to 40% of H(2*s*) and 60% of H(2*p*), while the doubly excited states are responsible for 50% of H(2*p*) and 50% of H(2*s*) [*Ajello et al.*, 1991].

Another important electron impact heat source is associated with vibrational excitation of the ground electronic state of H_2 following Lyman and Werner band transitions. We estimate the population of these excited states with a simplified version of the H_2 spectrum generator, described by *Dols et al.* [2000], for a temperature of 500 K and deduce an average vibrational energy of 2.8 eV per Lyman emission and 2.2 eV per Werner emission. Heat is produced since the time constant for vibrational relaxation is shorter than the radiative time constant for the vibrationally excited electronic ground state.

Collisions of suprathermal precipitating auroral electrons with thermal electrons is a source of heat for the thermal electron gas. The complete expression for the energetic electron-thermal electron energy loss rate was approximated by *Swartz et al.* [1971]. Since the ambient electrons transfer their energy to the neutral gas, all this energy is eventually transformed into neutral heat through efficient coupling of the electron thermal gas to H_2 rotational and vibrational excitation.

Considerable amounts of heat are released from exothermic chemical reactions involving production and loss of atomic

Table 1. List of Chemical Reactions, Exothermicities and Reaction Coefficients Involved in Chemical Heating Sources

Reaction	Reaction	Rate Coefficient, $cm^3\ s^1$	Reference
1	$H_2^+ + H_2 \rightarrow H_3^+ + H + 1.6$ eV	2.0×10^{-9}	*Theard and Huntress* [1974]
2	$H_3^+ + e \rightarrow H + H + H + 4.8$ eV	$1.15 \times 10^{-7} \left(\frac{T}{300}\right)^{0.65}$	*Datz et al.* [1995]
3	$\rightarrow H_2 + H + 9.3$ eV		*Sundström et al.* [1994]
4	$H + H + H_2 \rightarrow H_2 + H_2 + 4.48$ eV	$8 \times 10^{-33} \left(\frac{T}{300}\right)^{0.6}$	*Ham et al.* [1970]
5	$H_2^+ + e \rightarrow H + H + 10.95$ eV	1×10^{-8}	*Auerbach et al.* [1977]

hydrogen (Table 1). Once formed, H_2^+ ions react with H_2 to produce H_3^+ and H, thus breaking an H_2 bond. The H_3^+ ions recombine with electrons to yield either H_2 + H or H + H + H, along with excess kinetic energy. The H atoms ultimately recombine through three-body association with H_2.

The branching ratio of the two possible channels was measured by *Datz et al.* [1995]. They show that 75% of the H_3^+ ions follow the H + H + H pathway and 25% lead to H_2 + H. The temperature dependence of the H_3^+ recombination coefficient was measured by *Sundström et al.* [1994] (Table 1, reactions 2 and 3). Note that the H_2 + H pathway releases 9.3 eV, almost twice as much energy as the H + H + H pathway. The very efficient $H_2^+ + H_2$ reaction (Table 1, reaction 1) rapidly converts H_2^+ ions into H_3^+ ions with an energy release of 1.6 eV. The $H_2^+ + e \rightarrow H + H$ dissociative recombination (Table 1, reaction 5) is also considered. It is less efficient than reaction (1) but provides 10.95 eV to the ambient gas. These very large auroral heat sources generate strong thermospheric winds [*Sommeria et al.*, 1995; *Rego et al.*, 1999] that will globally redistribute both heat and neutral constituents like H. However, we have considered that this reaction chain, excepted three-body recombination of H, occurs in the same layer and that heat is produced at the same level. Comparison of the eddy diffusion lifetime with the chemical lifetime of the three-body recombination of H atoms with H_2 (Table 1, reaction 4) shows that above the homopause, the downward transport of H is more efficient than its recombination. Therefore the energy associated with the small fraction of recombination that would occur above the homopause in the absence of transport is redistributed below this level.

2.2.2. Unspecified heat sources. So far, we have considered heat sources resulting from auroral particle precipitation in the atmosphere; other nonauroral heat sources might play an important role in the temperature budget but have not been directly taken into account in this study. Joule heating generated by the presence of a perpendicular electric field in the presence of Pedersen conductivity is an important heating process in the auroral ionosphere (in the Earth atmosphere it represents almost 50% of the heating). Estimation of its effects deserves a complete parametric study of the Jovian ionospheric electric field vertical profile. It is out of the scope of this study and will be presented elsewhere.

Young et al. [1997] showed that the energy viscously dissipated by breaking gravity waves is comparable to that needed to heat the equatorial atmosphere. However, this conclusion was recently challenged by *Matcheva and Strobel* [1999], who found that gravity waves with amplitudes and properties consistent with those inferred from temperature variations in the Galileo probe temperature by *Young et al.* [1997] are unable to heat Jupiter's thermosphere sufficiently to account for the large temperature gradients and high temperatures derived from the probe data. Accordingly, the potentially produced heat has not been included in the present model.

The exothermic hydrocarbon chemistry may also play an important role in the stratosphere but this possibility has not been addressed in the code. As will be illustrated in section 6, these nonauroral heat sources are expected to balance the hydrocarbon cooling in the polar regions and to sustain the thermal profile observed in the equatorial regions. Their effect is, at least partly, mimicked by preventing the temperature, deeper than a critical pressure, to drop below the initial temperature profile.

2.3. Heat Sinks

Altitude-dependent radiative cooling by thermal infrared band emissions from H_3^+, CH_4, and C_2H_2 is considered following the method described by *Drossart et al.* [1993a]. For each molecule, radiation is calculated for the fundamental transition that is predominant in the infrared spectrum. We assume that the hydrocarbon auroral emissions originate in optically thin layers and use a simple radiative transfer model (cooling to space approximation) to calculate thermal emission rates as a function of altitude for the ν_4 band of CH_4 (1306 cm^{-1}) and the ν_5 band of C_2H_2 (729 cm^{-1}). For the H_3^+ ν_2 band (2521.31 cm^{-1}) a method similar to that used for the hydrocarbons is adopted, it makes use of the high-temperature partition function from *Neale and Tennyson* [1995]. The correction due to nonlocal thermodynamic effects depends on the vibration-vibration (*V-V*) and vibration-translation (*V-T*) transfer quenching rates for each molecule. We solely consider quenching by H_2 (which is dominant in the stratosphere or lower ionosphere). Temperature dependent quenching rates are taken to be the same for all hydrocarbons. The "phenomenological" reaction rate coefficient of 2.7×10^{-10} $cm^3\ s^{-1}$ derived by *Kim et al.* [1974] is used for the quenching of H_3^+ by H_2.

In the local thermodynamic equilibrium (LTE) approximation the infrared emission of H_3^+, CH_4 and C_2H_2 are proportional to the number of molecules in the first vibrational level, which is an increasing function of temperature. A non-LTE correction factor is used [*Drossart et al.*, 1993a] which depends on the quenching rate for each molecule. It does not significantly modify this temperature dependence, and therefore the radiative cooling efficiencies are proportional to the gas temperature.

3. Initial Energy Distribution of the Auroral Electrons

We consider two auroral electron energy distributions meant to reproduce the effects of (1) a diffuse, unstructured aurora, usually observed in the polar cap and afternoon sectors of the northern auroral region and (2) a bright discrete arc generally present in the morning sector of the northern auroral region.

The energy distribution of the electrons giving rise to a diffuse aurora is obtained by fitting measured Galileo Energetic Particle Detector (EPD, *Williams and McEntire,* 1992] near-isotropic distributions with a kappa function [*Bhattacharya et al.*, 1998]. The near-isotropic distribution in the equatorial magnetosphere implies a loss cone that is filled as a result of plasma wave scattering of energetic particles, which subsequently precipitate into the atmosphere. The kappa distribution combines a power law distribution for high-energy electrons and a linear distribution for the low-energy electrons. The fit parameters are derived from multiple fits to the EPD energetic electron distribution measured between 10 and 20 R_J.

By analogy with the Earth case we consider that the electron beam responsible for the diffuse aurorae is accelerated in the equatorial plane of the magnetosphere and is not subject to further acceleration during its travel along magnetic field lines. Therefore it is reasonable to assume that for the diffuse auroral case, the electron energy distribution deduced from the Galileo observations in the equatorial magnetosphere is representative of the energy distribution of the electrons impinging on the Jovian atmosphere.

The EPD instrument is designed to measure the spectra and angular distributions of electrons with energy above 15-keV and is therefore not sensitive to low-energy electrons that are known to be responsible for heating the upper atmosphere and produce the EUV emission observed with HUT [*Wolven and Feldman*, 1998] and the Galileo Extreme Ultraviolet Spectrometer [*J.M. Ajello et al.,* Spectroscopic evidence for high altitude aurora at Jupiter from Galileo Extreme Ultraviolet Spectrometer and Hopkins Ultraviolet Telescope observations, submitted to Icarus, 2000]. Even though the actual distribution is probably characterized by a complex shape, we have assumed that this low-energy part of the distribution may be represented by a double-Maxwellian distribution, compatible with two pools of electrons in thermal equilibrium.

We have represented the initial energy flux distribution for the diffuse auroral case with the form:

$$\phi(E)=\alpha\phi_{0,1}\frac{E}{E_{0,1}}\left(1+\frac{E}{\kappa}E_{0,1}\right)^{-\kappa-1}+\beta\phi_{0,2}\frac{E}{E_{0,2}}\exp\left(-\frac{E}{E_{0,2}}\right)+\gamma\phi_{0,3}\frac{E}{E_{0,3}}\exp\left(-\frac{E}{E_{0,3}}\right)$$

where α, β and γ are normalization constants; $\phi_{0,1}$, $E_{0,1}$, and κ and are the energy flux, the characteristic energy, and the kappa index associated with the kappa distribution, respectively; $\phi_{0,2}$, $\phi_{0,3}$, $E_{0,2}$, $E_{0,3}$ and are the energy fluxes and the characteristic energies associated with the double Maxwellian soft electron energy distribution. This initial distribution has the following parameters: $\phi_{0,1}$ = 20 erg cm^{-2}s^{-1}, $E_{0,1}$ = 15 keV, κ=2.1; $\phi_{0,2}$ = 10 erg cm^{-2}s^{-1}, $E_{0,2}$ = 3 keV; $\phi_{0,3}$ = 0.5 erg cm^{-2}s^{-1}, $E_{0,3}$ = 100 eV.

The energy distribution of the electrons giving rise to a discrete aurora is determined by the need to meet the different constraints such as the altitude of the peaking H_2 visible emission observed in an auroral arc by Galileo, the FUV color ratio, and the large measured intensities in the auroral arcs.

The discrete arcs observed in the Earth's aurora are generated by electrons accelerated by potential drops along the magnetic field lines. Such accelerated electron beams were detected in the outer Jovian magnetosphere during the Ulysses flyby of Jupiter in 1992 beyond 15 R_J and near the magnetopause. In particular the Ulysses magnetometer observed changes of magnetic field associated with sheets of field-aligned currents near 15 and 20 R_J in the dusk sector [*Dougherty et al.*, 1993]. In absence of in situ measurements of the precipitating flux at the top of the atmosphere we represent it with a triple Maxwellian distribution. The soft electron Maxwellian distribution is similar to the double Maxwellian component used for the diffuse aurora, while the high-energy component is adjusted to match the observational constraints, as explained in the following sections.

The initial energy flux distribution has the form

$$\phi(E)=\alpha\phi_{0,1}\frac{E}{E_{0,1}}\exp\left(-\frac{E}{E_{0,1}}\right)+\beta\phi_{0,2}\frac{E}{E_{0,2}}\exp\left(-\frac{E}{E_{0,2}}\right)+\gamma\phi_{0,3}\frac{E}{E_{0,3}}\exp\left(-\frac{E}{E_{0,3}}\right),$$

where α, β, and γ are normalization constants; $\phi_{0,1}$ and $E_{0,1}$ are the energy flux and the characteristic energy of the high-energy Maxwellian distribution; $\phi_{0,2}$, $\phi_{0,3}$ and $E_{0,2}$, $E_{0,3}$ are the energy fluxes and the characteristic energies associated to the double Maxwellian soft electron energy distribution.

The initial distribution is illustrated in Figure 2 for $\phi_{0,1}$ = 100 erg cm^{-2}s^{-1}, $E_{0,1}$ = 22 keV; $\phi_{0,2}$ = 10 erg cm^{-2}s^{-1}, $E_{0,2}$ = 3 keV; $\phi_{0,3}$ = 0.5 erg cm^{-2}s^{-1}, $E_{0,3}$ = 100 eV.

4. Observational Constraints

The values of observable quantities such as the altitude of the H_2 emission peak, IR and UV emissions, and temperatures associated with various optical signatures are used to constrain the parameters of the energy distribution of the precipitating electrons:

1. A domain of observational constraints on the auroral temperature profile is constructed from multispectral analysis of the auroral region emissions,

2. A mean FUV emission rate deduced from auroral spectra and images is used to provide an order of magnitude for the total precipitated energy, while the emission profile (including H_2 visible emission) gives important clues on the altitude distribution of the auroral particle energy deposition and more specifically on the altitude of the H_2 emission peak.

3. FUV color ratio and the associated CH_4 column density are used to indicate the penetration depth of the degraded beam below the methane homopause.

4. IR emission processes are diagnostics of the cooling processes in the mesosphere from CH_4 and C_2H_2 at wavelengths between 7 and 14 microns and also an important diagnostic of the upper thermosphere and ionosphere from H_3^+ emission near 3.5 microns.

It should be noted that all these observations were not simultaneous in time and space and do not necessarily stem from similar processes. Knowing the temporal and spatial variability of the Jovian aurora, one needs to be careful when comparing

quantities resulting from different mechanisms and appearing at different times and locations.

4.1. Thermal Profile

A range of observational constraints on the auroral temperature profile may be constructed from observations spanning three different overlapping pressure level regions (shaded regions in Figure 3).

The first region, between 10^{-3} and 10^{-6} bar, is constrained by the hydrocarbon (mainly CH_4 and C_2H_2) thermal infrared emissions observed with the Voyager IRIS and reanalyzed by *Drossart et al.* [1993a]. They derived two temperature profiles based on different CH_4 density profiles: (1) a warm boundary corresponding to the best fit for hydrocarbon emission for the hydrocarbon distribution derived from Voyager UVS observation, (2) a cold boundary inferred from the thermal profile derived from the hydrocarbon distribution of *Gladstone* [1982]. *Kostiuk et al.* [1993], and *Livengood et al.* [1993] derived a warmer thermal profile in the 10^{-3}-10^{-6} bar pressure region from C_2H_4 and C_2H_6 IR emissions observed with the Infrared Telescope Facility on Mauna Kea.

The second region constraining the temperature profile is defined by the temperature derived from H_2 FUV auroral emission. Different H_2 rovibrational temperature ranges have been derived by fitting synthetic spectra to various spectral ranges observed with GHRS [*Trafton et al.*, 1994, 1998; *Clarke et al.*, 1994; *Liu and Dalgarno*, 1996; *Kim et al.*, 1997; *Dols et al.*, 2000]. These measurements define a H_2 temperature range of 400-850 K corresponding to emissions occurring between the 10^{-5} and 10^{-8} bar levels.

The third region (700-1100 K) can be defined on the basis of the temperatures inferred from the H_3^+ near-IR emission [*Drossart et al.*, 1989; *Maillard et al.*, 1990; *Lam et al.*, 1997]. They define an ionospheric temperature range of 700-1100 K for the region where the H_3^+ emission originates, that is approximately between the 10^{-6} and 10^{-10} bar levels.

The effective H_2 temperature has been deduced from the H_2 UV rovibrational spectra and from the IR line of H_2 quadrupole emission. In this model it is estimated by weighting the temperature profile with the calculated H_2-FUV emission rate profile. A similar method is applied to estimate the H_3^+ temperature from the calculated H_3^+ emission profile.

4.2. UV Emission

Total Lyman band emission rates of 20-270 kiloRayleighs (kR) have been measured by *Kim et al.* [1997] over the Large Science Aperture (LSA) of the GHRS spectrometer. The estimated total Lyman band intensity depends on the filling factor of the auroral emission in the LSA. The authors have assumed that the LSA aperture is completely filled with the auroral emission; however, recent UV images [*Clarke et al.*, 1998] have revealed thin bright auroral structures (~ 1000 km wide) that only partially fill the LSA. Although we have no information on the filling factors at the time of the observations, it can be estimated that a filling factor of 20%, compatible with a 1000-km-wide auroral arc, would give rise to total H_2-FUV auroral emission intensities of the order of 200-2700 kR. *Trafton et al.* [1998] and *Dols et al.* [2000] obtained similar GHRS spectra with total integrated intensity (Lyman and Werner bands) averaged over the aperture varying from 50 to 400 kR. These derived apparent emission rates are attenuated by hydrocarbon absorption and also assumed that the aperture is fully filled with auroral emission. A filling factor of 20% would then give rise to apparent emission rates of 250-2000 kR. *Morrissey et al.* [1997] measured a mean H_2 brightness of 106 kR with HUT; however, these measurements suffer from large uncertainties on the auroral area integrated in the aperture. From these observations it can be assumed that a diffuse aurora usually fully fills the aperture of the detector and gives rise to a typical vertical total H_2 brightness of 300 kR in the 900-1700 Å bandpass. A discrete aurora, on the other hand, generally only partly fills the aperture and a typical total H_2 brightness of 1 MR may be assumed.

Little information on the FUV vertical emission profile has been deduced so far from images taken by the FOC and the WFPC2 on board HST. The emission profile can only be determined at the limb where the apparent brightness distribution is controlled by the viewing geometry, the spatial limitations of HST, and the instrument's point spread function (PSF) [*Grodent et al.*, 1997; *Gérard et al.*, 1998]. Galileo images taken during orbit G7, however, show that the H_2 visible emission profile of an auroral arc is characterized by a vertical full width at half maximum of 120 ±30 km [*Vasavada et al.*, 1999] and drops below the detection limit at a full width of 350 ±70 km. The altitude of this auroral nightside emission has been determined to be 245 ±30 km above the 1 bar level. *James et al.* [1998] have shown that these visible-wavelength emissions could be ascribed to the H_2 ($a3 \rightarrow b3$) continuum, together with strong lines assigned to the radiative decay of the gerade singlet states of H_2, and to members of the H Balmer series resulting from dissociative excitation of H_2. Since these emissions are presumably also excited by auroral electron impact on H_2, it is assumed that the H_2 FUV and the visible emissions peak at the same altitude.

The UV emission profile can also be constrained by the H_2 - FUV color ratio. As explained below, this constraint gives some indication on the distribution of the emission profile above and below the homopause.

4.3. Color Ratio and CH_4 Column Density

The H_2 -FUV color ratio C =[I (1550–1620)]/ [I (1230–1300)] is related to the considerable drop in the CH_4 absorption cross section at wavelengths above 1350 Å [*Yung et al.*, 1982; *Harris et al.*, 1996; *Gérard et al.*, 1998]. It leaves the bulk of the longer wavelength H_2 Lyman band emissions unattenuated, while the Werner and Lyman band emissions at wavelengths less than 1350 Å are substantially absorbed by methane. The color ratio C is calibrated to give a value of 1.1 for an unattenuated H_2 spectrum, compatible with the value derived from the laboratory spectrum for 100-eV electrons on H_2 obtained by *Liu et al.* [1995]. The color ratio is linked to the ratio of emission above and below the homopause and is therefore a proxy for the penetration depth of the electron beam below the homopause. In order to evaluate the color ratio associated with the energy distribution of the precipitating electrons, a synthetic spectral generator is used to calculate the UV emission intensity in a prescribed spectral band for each atmospheric layer [*Dols et al.*, 2000].

At the temperature of the Jovian atmosphere the H_2 molecules in the ground state are mostly in the ground vibrational level (v''=0). The population of the vibrational levels (v') of the B, C and EF states, excited by the electron impact, are calculated with the analytical energy dependent excitation cross sections from *Shemansky et al.* [1985] updated by *Liu et al.* [1998]. The transition probabilities from these excited states to the ground level are taken from *Abgrall et al.* [1999]. The corresponding wavelengths of these transitions are deduced from the calculated

energy levels from *Dabrowsky et al.* [1984]. At each altitude step a spectrum is generated, depending on the local electron energy distribution calculated with the energy degradation model and H_2 density. In order to account for the continuum emission the spectra are normalized to the column excitation rate of the *B*, *EF* and *C* levels from the ground levels. The synthetic spectra generated at each altitude step are attenuated by absorption from the overlying methane column and integrated along a line of sight. A wavelength dependent CH_4 absorption cross section [*Mount and Moos*, 1978] is used along with the methane density profile calculated by the model.

On the basis of 11 eleven years of IUE spectral observations, *Harris et al.* [1996] have deduced an average color ratio of 2.5 in the north corresponding to the best linear fit to auroral H_2 archival bandpass intensities. Galileo FUV observations in the Northern Hemisphere provide a similar mean value (W. R. Pryor, private communication, 1999). The color ratio is often expressed in terms of a corresponding vertically integrated CH_4 column density above the emission peak. This integrated column only depends on the CH_4 density profile and can be directly used to attenuate any bandpass of the H_2 UV spectrum. It should be noted, however, that it assumes that all the emission is concentrated at the emission peak overlaid by a methane absorbing layer. *Kim et al.* [1997] observed high-resolution GHRS spectra of the aurora in the two wavelength ranges 1257-1293 Å and 1587-1621 Å and estimated methane column densities in the range (1.5-6.5)x10^{16} cm^{-2}, corresponding to a color ratio range of 1.5-3.6.

4.4. Thermal IR Emissions

Drossart et al. [1993a] estimated the hydrocarbon IR excess emission from IRIS *Voyager* observations in the northern auroral hot spot. These emissions were viewed at ~ 60° emission angle, and the IRIS projected field of view was 23,000 km in latitude and 11,500 km in longitude, that is, larger than the auroral hot spot, i.e., a region of enhanced polar emissions in the 7.8-μm spectral region [*Caldwell et al.*, 1980]. They deduced CH_4 and C_2H_2 IR emissions, integrated over 2π and averaged over the global IRIS field of view, of 93 ± 9 and 86 ± 5 ergs cm^{-2} s^{-1}, respectively. They correspond to a filling factor of the aperture by the auroral emission of the order of 0.4. Therefore both emission rates are estimated to be of the order of 300 ergs cm^{-2} s^{-1}. The assumption of an optically thin hydrocarbon emission layer restricts the range of pressure to which their model can be applied. It is roughly defined by the pressure levels corresponding to a CH_4 integrated column of 5.3x10^{17} cm^{-2} and a C_2H_2 integrated column of 7x10^{15} cm^{-2}, respectively. We use these column densities to determine the altitude at which the thermal IR radiation is able to leave the hydrocarbon layer. For the diffuse auroral case the altitudes of unit optical depths for CH_4 and C_2H_2 layers are 226 km (1.6x10^{-5} bar) and 196 km (4.x10^{-5} bar).

Lam et al. [1997] observed the H_3^+ infrared auroral emission with the United Kingdom Infrared Telescope (UKIRT) high spectral resolution instrument. They observed a total emission power (integrated over 4π) corrected for line-of-sight effects of the order of 1.5 erg cm^{-2} s^{-1} at 60°, corresponding to an H_3^+ column density 2.5-12.5x10^{+12} cm^{-2}. These values were averaged over a 3" x 3" pixel, which covered an area on Jupiter of ~ 9800 x 9800 km^2 at the time of the observations. Analysis of H_3^+ imaging by *Satoh et al.* [1996] suggests a complex auroral structure similar to the structure observed in FUV. Hence, in the case of a discrete arc aurora a filling factor of ~ 20% may be considered, leading to an average emission power of 7.5 erg cm^{-2} s^{-1} corresponding to an H_3^+ column density 1.25-6.25x10^{+13} cm^{-2}. It should also be stated that since this thermal emission is dependent on both temperature and column density, a single emission spectrum can be fitted by different temperature/column density pairs. It is therefore impossible to determine the temperature and the column density independently from an observed spectrum. *Lam et al.* [1997] observed confined auroral zones showing a strong anticorrelation between temperature and column density. A strong H_3^+ IR emission is therefore not necessarily related to a high temperature.

It should be stated again that no simultaneous H_3^+ or hydrocarbon IR and H_2-FUV auroral emission data sets are currently available. The relationship between these emissions, probing different altitude regions and excited by different mechanisms, has therefore never been directly observed. The spatial-temporal variability of the H_2-FUV emission is not necessarily directly linked to the variability of the hydrocarbon and H_3^+ IR thermal emissions. Nevertheless, simultaneous use of the UV and IR average emissions is still of considerable interest to constrain the radiative signature of a general energy distribution, compatible with the thermal profile.

5. Initial Model Atmosphere

The initial model atmosphere is based on an analytical fit using a Bates function fitted to the thermal profile determined by *Seiff et al.* [1998] from the Galileo probe data (Figure 1). This thermal profile was calculated from measured densities with an exospheric temperature of 900 K. Altitudes are calculated from pressures and temperatures by integrating the hydrostatic equilibrium equation. The reference altitude corresponds to a pressure level of 1 bar, and we use the value of the acceleration of gravity at 60°N at thermospheric altitudes.

As a consequence of the previously described heating processes, precipitating auroral electrons modify the thermal profile of the Jovian thermosphere. In order to self-consistently account for the adjustment of the densities to the new temperature profile, the code iteratively solves the diffusion equations for H_2, He, H, CH_4, and C_2H_2. We use the general equilibrium distribution equation from *Banks and Kockarts* [1973, equation 15.17], which assumes an equilibrium between mixing and diffusive equilibrium.

This equation is solved with a two-point Gauss-Legendre quadrature method for H_2, He, and H. For H_2 and He the boundary mixing ratios at the bottom of the model atmosphere are 0.864 and 0.136, respectively [*von Zahn et al.*, 1998]. For pressures greater than 2.5x10^{-7} bar, we adopt the H mixing ratio profile derived by *Drossart et al.* [1993a]. The CH_4 boundary mixing ratio at the bottom of the model atmosphere is also taken from *Drossart et al.* [1993a]. The methane diffusion equation is solved with an eddy diffusion coefficient set as a free parameter that defines the altitude of the CH_4 homopause and of the FUV unit optical thickness. In the base model the eddy coefficient is set to 1.4x10^6 cm^2 s^{-1} [*Gladstone et al.*, 1996]. For pressures greater than 3.2x10^{-6} bar, we adopt the C_2H_2 mixing ratios derived by *Drossart et al.* [1993a]. Above this level, acetylene is distributed according to the general diffusion equation.

The H_3^+ density is estimated by assuming photochemical equilibrium. Since all H_2^+ ions produced are rapidly transformed into H_3^+, the H_3^+ production can be approximated by the H_2^+ production. By assuming charge neutrality and since H_3^+ is the major ion species in this highly aurorally excited ionosphere, the electron density is approximated by the H_3^+ density.

Three major H_3^+ loss terms have been considered: (1) $H_3^+ + e \rightarrow H_2 + H$ or 3H, with a reaction rate coefficient described in Table

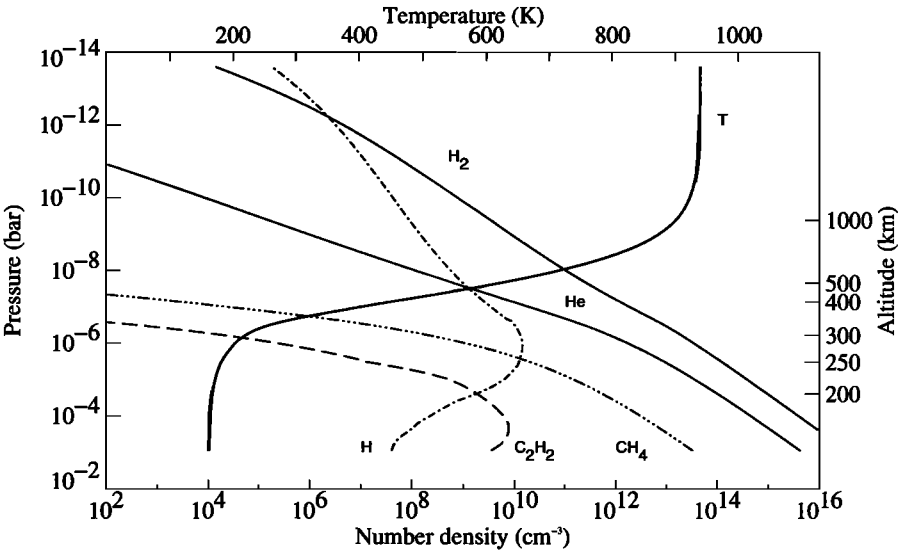

Figure 1. Initial model atmosphere: the temperature profile is an analytical fit to the equatorial thermal profile determined from the Galileo probe data adapted to the larger acceleration of gravity at 60° N and thermospheric altitudes. The density profiles are calculated as discussed in the text.

1; (2) $H_3^+ + CH_4 \rightarrow CH_5^+ + H_2$, k=2.4x10^{-9} cm^3 s^{-1} [*Kim et al.*, 1974]; and (3) $H_3^+ + C_2H_2 \rightarrow C_2H_3^+ + H_2$, k=3.5x10^{-9} cm^3 s^{-1} [*Kim et al.*, 1974]. The resulting density profiles are shown in Figure 1, where the H_3^+ density is estimated from the ionization produced with the energy distribution of the diffuse auroral case and the atmospheric structure appropriate to the Galileo thermal profile.

Since the temperature profile, the atmospheric composition, and the heating and cooling efficiencies are intimately related, an iterative approach must be adopted to calculate the steady state of the atmosphere under auroral precipitation. The heating and cooling vertical profiles are calculated at each time step. The energy balance equation resulting from the energetic electron energy deposition is then iterated with the new temperature and density profiles until stable steady state temperature and density profiles are achieved.

6. Model Results

6.1. Local Electron Energy Flux

Figure 2 illustrates the altitude dependence of the energy spectrum of the auroral electron flux (upward + downward) for the discrete auroral case. As the primary electron beam reaches deeper pressure levels, the electrons degrade their energy, partly backscatter, and produce secondaries. Four altitude levels are

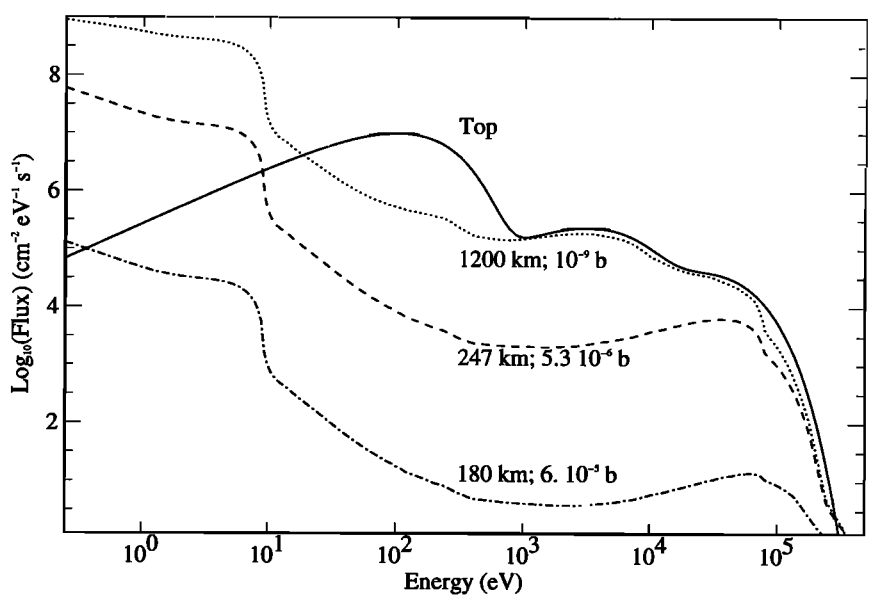

Figure 2. Evolution of the discrete auroral energy flux distribution as the electron beam penetrates into the atmosphere. Four altitude levels are considered: initial energy distribution at the top of the atmosphere (solid line), degraded energy distribution above the H_2 emission peal: (1200 km) (dotted line), at the emission peak (247 km) (dashed line), and below the emission peak (180 km) (dashed-dotted line).

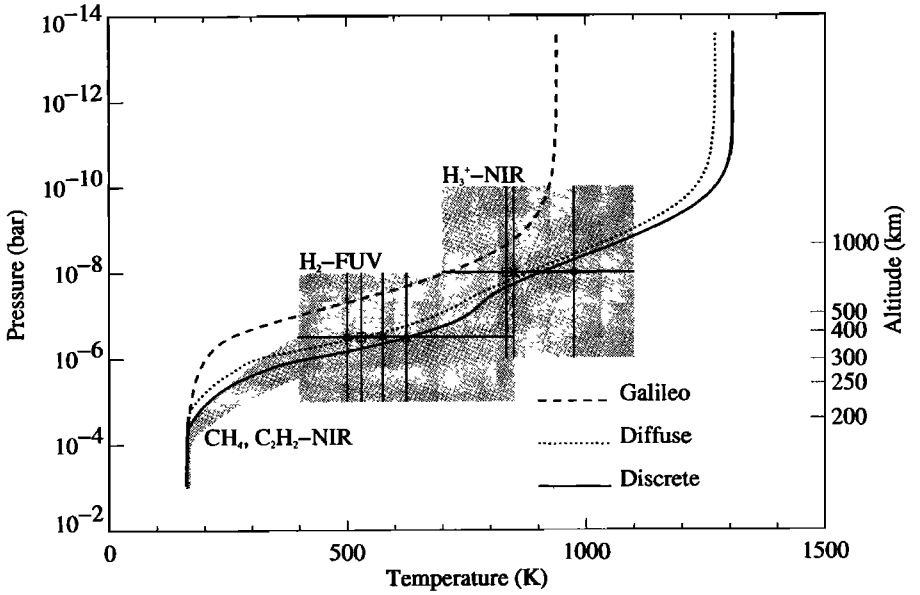

Figure 3. Temperature profiles calculated for the diffuse and discrete auroral cases. The Galileo equatorial temperature profile is shown for comparison. The altitude axis refers to the Galileo atmosphere. The shaded areas are the regions of observational constraints. The first shaded region (between 10^{-3} and 10^{-6} bar) is derived from hydrocarbon (CH_4 and C_2H_2) NIR thermal emissions in an auroral hot spot. The second shaded region (between 10^{-5} and 10^{-8} b) is defined from H_2-FUV auroral spectra (diamond, *Liu et al.*, [1996]; square: *Trafton et al.*, [1994, 1998]; cross: *Clarke et al.*, [1994]; triangle: *Kim et al.*, [1997]. The third shaded region (between 10^{-6} and 10^{-10} bar) is inferred from H_3^+ -NIR emission in the aurora (square: *Maillard et al.*, [1990]; cross: *Lam et al.*, [1997; diamond: *Drossart et al.*, [1989].

illustrated: (1) initial energy distribution at the top of the atmosphere, (2) degraded energy distribution above the H_2 emission peak (1200 km), (3) at the H_2-FUV emission peak (247 km), and (4) below the emission peak (180 km). The flux profiles result from the balance between production and loss into the different energy bins. Since all degrading processes occur simultaneously, it is difficult to discriminate their individual action. The degradation rate of the electron flux along its path is mainly controlled by the behavior of the H_2 density profile. Below the level of the peak of H_2 emission, corresponding to the level of maximum energy deposition, the electron flux rapidly vanishes. This level is determined by the shape of the initial energy distribution of the electrons; in the case of a monoenergetic electron beam, the pressure level of the peak is proportional to the energy, and for more complex distributions, the altitude mainly depends on the mean or characteristic energy.

The shape of the electron fluxes in Figure 2 can be discussed with simple considerations. For energies higher than 20 eV the total electron interaction cross section rapidly decreases, resulting in a slower degradation of high-energy electrons (>5 keV). An efficient depopulation of the low-energy bins occurs at all altitudes, and the soft electrons having a mean energy of ~100-eV, which corresponds to the maximum of the degradation cross section, rapidly vanish as the electron beam, penetrates into the atmosphere. However, this depopulation is partly balanced by the massive arrival of low-energy secondaries with energies < 1 keV. Indeed, with a mean energy per ion pair of 40-eV, one 40-keV electron is able to produce ~ 1000 secondary electrons, which will rapidly populate these low-energy bins. The abrupt rise of the electron flux below 10-eV corresponds to a minimum in the total inelastic cross section between rotational and vibrational excitation and other processes having a threshold energy of the order of 10-eV. In order to avoid numerical problems we assume that all cascading energy that populates the lowest-energy bin (0.25-eV) is ultimately converted into electron heating.

6.2. Temperature Profile

Figure 3 shows the vertical temperature profiles obtained with the diffuse and discrete auroral energy distributions. In both cases, the convergence process used a temperature increment of 1 K per time step above the critical pressure (set to 1 μb) and of 0.5 K below it. The profiles are compared with the Galileo equatorial thermal profile and with the temperature constraints (shaded regions in Figure 3) deduced from the UV and IR auroral emissions.

It is directly seen that above the homopause (~1 μbar), both thermal profiles are in agreement with the H_2-FUV and H_3^+-NIR constraints, while below the homopause only the discrete auroral energy distribution agrees with the hydrocarbon-NIR constraints. As expected, the nonauroral Galileo thermal profile is too cold, especially below the homopause. Numerical values of relevant temperatures are listed in Table 2.

An exospheric temperature of ~1300 K is reached in both cases, higher than the temperature deduced from Galileo for the equatorial exosphere (940 K). The H_2 temperature is 407 K in the discrete auroral case, just at the lower limit of the H_2-FUV temperature constraint (400-800 K), and reaches 473 K in the diffuse auroral case, in better agreement with the observational range. The H_3^+ temperature is estimated in the same way by weighting the thermal profile with the H_3^+-NIR emission profile. The diffuse and discrete auroral energy distributions give rise to the same H_3^+ temperature of 740 K, which is in the lower part of the observational range (700-1100 K).

The similarities between the discrete and diffuse thermal profiles, especially above the homopause, are apparently in

Table 2. Main Outputs Resulting From the Energy Degradation of the Diffuse and Discrete Auroral Cases Compared With Observations

	Observation	Diffuse Auroral Case	Discrete Auroral Case
Exospheric temperature, K	940	1271	1309
H_2 temperature, K	400-800	473	407
H_3^+ temperature, K	700-1100	739	744
Vertically integrated H_2 excitation, kR	300 (diffuse) 1000 (discrete)	295	1100
H_2 emission peak altitude, km	245 (± 30)	245	247
CH_4 homopause altitude, km	321	312	320
H_2 FUV color ratio (60°)	1.5-3.6	1.33	1.63
Integrated CH_4 column (10^{16} cm^{-2})	1.5-6.5	1.1	2.1
Integrated H_3^+ emission (60°), erg cm^{-2} s^{-1}	1.5 (diffuse) 7.5 (discrete)	11	23
H_3^+ column, (10^{12} cm^{-2})	2.5-12.5 (diffuse) 12.5-62.5(discrete)	18	25
Integrated CH_4 emission (60°), erg cm^{-2} s^{-1}	93 (± 9) (diffuse) 300 (discrete)	47	170
Integrated C_2H_2 emission (60°), erg cm^{-2} s^{-1}	86 (± 5) (diffuse) 300 (discrete)	15	23

contradiction with the large difference existing between the total energy fluxes, which is 110.5 erg cm^{-2} s^{-1} for the discrete distribution and 30.5 erg cm^{-2} s^{-1} for the diffuse auroral case. However, it will be shown that the heat released by the three components of the energy distributions is confined in different altitude regions, the higher the energy of the electron beam, the deeper the level it is released. Since the soft electron components are the same in both cases, it is not surprising that the upper parts of the thermal profiles are similar. It will also be shown that the heat released by the high-energy component is partly balanced by the hydrocarbon IR cooling and, even if the hard electron component of the discrete auroral case is 5 times more important than in the diffuse auroral case, it does not give rise to a strong temperature difference.

6.3. H_2^+ and H^+ Production Rate Profiles

The ionization produced by the electrons of the discrete auroral case is illustrated in Figure 4. The integrated ion production rates from the various processes are listed in Table 3.

H_2^+ has the major ion production rate in the Jovian ionosphere, ~ 1 order of magnitude higher than the dissociative ionization rate of H_2. However, the efficient reactions described in Table 1 rapidly convert this ion into H_3^+ which is dominant in the Jovian ionosphere. The H^+ production rate from dissociative ionization of H_2, hereafter denoted H+(H_2), is ~ 2 orders of magnitude higher than the H^+ production rate from direct ionization of H, hereafter H+(H). Finally, the He^+ integrated production rate is about half of the H+(H_2) rate.

Figure 4 allows us to discriminate the contribution of the three Maxwellian components and may give some clues on the penetration depth of the electron beam as function of the characteristic energy of the energy distribution. The 100-eV component gives rise to a local maximum around 10^{-10} bar (~1300 km), which is best seen for the H+(H) ion production rate. The 3-keV component does not present a sharp peak, but the level of maximum ionization can be estimated at the inflection point of the H+(H_2) rate profile, around 10^{-7} bar (~550 km). The high-energy component (22-keV) is responsible for the major maximum located at 10^{-5} bar (~250 km). Accordingly, half of the energy is deposited below the methane homopause.

The H+(H_2) production rate profile has a shape similar to the H_2^+ production rate profile. On the other hand, the H^+(H) and He^+ production rate profiles are different: while H^+(H) is mainly formed at high altitude by the two soft electron components, the He^+ ion is preferentially produced at lower altitude by the high-energy component. This is readily explained by the changing chemical composition as altitude increases in the thermosphere, which leads to a large fractional abundance of H at high altitude and to a decreasing fractional abundance of He as altitude increases above the homopause.

The average energy to create an ion pair is 42-eV, slightly higher than the 37-eV derived from laboratory measurements in a pure H_2 atmosphere. This difference stems from the low-energy electrons that do not have sufficient energy to ionize the gas while they contribute to the total energy flux of the beam and from the slightly different chemical composition of the atmosphere.

6.4. Heating and Cooling

The cooling and heating rate profiles obtained with the discrete auroral energy distribution are shown in Figure 5. As already mentioned, we consider the cooling terms associated with thermal IR radiations from H_3^+, CH_4, and C_2H_2. These molecules cool different regions of the atmosphere because the heavier hydrocarbon molecules are mostly confined below the homopause (320 km), while the H_3^+ ion, which is destroyed by hydrocarbons below the homopause, is mostly present above the homopause.

Turbulent transport controls the CH_4 density and therefore plays an important role in the cooling rate in the vicinity of the homopause, that is, in the region including the level of maximum energy deposition. The effect of the eddy coefficient on the thermal profile and on the absorption of H_2-FUV emission by CH_4 will be discussed in the sensitivity studies. H_3^+, on the other hand, mainly controls the ionospheric region of the temperature profile and directly regulates the H_3^+ and exospheric temperatures.

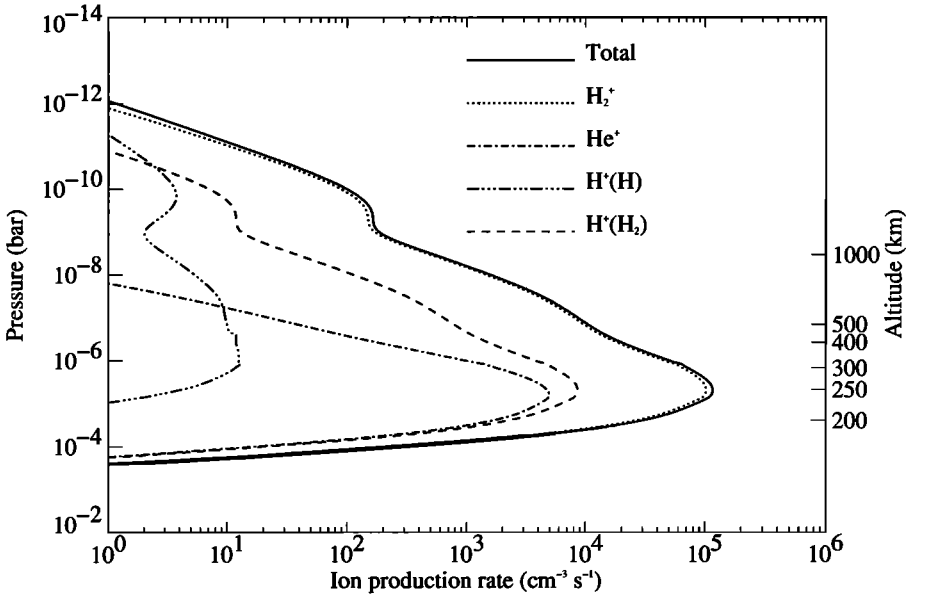

Figure 4. Ion production rates as a function of altitude and pressure for the discrete auroral energy distribution. The plot shows the total ion production (solid line), the H_2^+ production (dotted line), the He^+ production (dashed-dotted line) and the H^+ production resulting from direct ionization of atomic hydrogen (dash-dot-dot line) and from dissociative ionization of H_2 (dashed line).

Table 4 lists the contributions of the different heat sources to the total heating. For the diffuse and discrete auroral energy distributions, 50% of the total auroral input electron energy is converted into heat in the atmosphere.

In this model, heating of the Jovian atmosphere is largely dominated by chemical heating which results from the reaction chain initiated by the ionization of H_2. The excitation of the vibrational and rotational levels of the ground state of the H_2 molecule is the second most important heat source. Its importance reflects the large excitation cross sections of these processes occurring at low energies for which energy bins are highly populated. The heat produced by the dissociation of excited H_2 singlet and by excitation of the H_2 ground level following radiative transition from the *B* and *C* electronic states are comparable. These two processes are linked as they both result from deexcitation of excited singlet states. The heat released by H_2 dissociation from doubly excited states represents a marginal contribution to the total because of the high threshold energies of these processes and their low cross sections.

The imbalance between heat sources and heat sinks is accounted for by downward heat conduction that gives rise to the thermal profiles for the diffuse and discrete aurora presented in Figure 3.

The auroral heat vertical distribution is intimately related to the shape of the energy distribution. Figure 3 shows that the 22-keV component heats a region of the homosphere between 10^{-4} and 10^{-6} bar and has an important effect on the H_2 temperature (the same observations apply to the kappa component of the diffuse distribution). The 3 -keV component heats the region directly above the homopause, between 10^{-6} and 10^{-9} bar and has the largest influence on the H_2 and H_3^+ temperatures. The 100-eV component is mostly responsible for the net heating in the thermosphere, from 10^{-9} to 10^{-12} bar. Since the IR cooling is no longer efficient above 10^{-10} bar, the energy flux contained in the 100-eV component does not have to be large (0.5 erg cm^{-2} s^{-1}) to produce a large exospheric temperature. It has a moderate effect on the H_3^+ temperature. This soft electron component was initially suggested by *Hunten and Dessler* [1977]. They showed that one possible source of heat input in the Jovian thermosphere

Table 3. Integrated Auroral Production Rates of the Major Ions

	Integrated Production Rate, cm^{-2} s^{-1}	
Ion Produced	Diffuse	Discrete
H_2^+	4.1×10^{11}	1.45×10^{12}
H+(H_2) dissociative ionization	3.4×10^{10}	1.2×10^{11}
H+(H) direct	6.9×10^{8}	9.9×10^{8}
He^+	8.9×10^{9}	4.5×10^{10}
Total	4.6×10^{11}	1.65×10^{12}

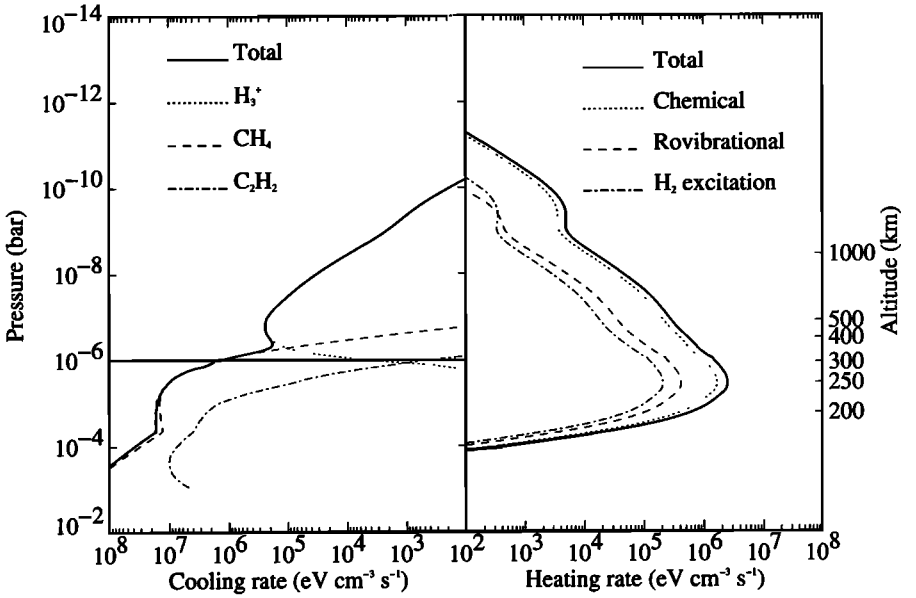

Figure 5. (left) Cooling and (right) heating rate (right plot) profiles resulting from the energy degradation of the discrete auroral energy distribution. The cooling rate profiles from H_3^+ (dotted), CH_4 (dashed) and C_2H_2 (dashed-dotted line) are shown with the total cooling rate profile (solid) on the left side. The horizontal line at 10^{-6} bar represents the critical pressure below which only heating of the atmosphere is allowed (see text). The right side of the plot shows the total heating rate profile (solid), the chemical (dotted line) and rovibrational (dashed line) heating rate profiles, along with the heating rate profile resulting from H_2 excitation (dashed-dotted line).

may be the precipitation of 0.25-0.5 erg cm^{-2} s^{-1} from a warm plasma (30-500 eV).

In the homosphere, heat is very efficiently transferred into hydrocarbon cooling, and therefore the high-energy component does not necessarily give rise to a substantial temperature increase. This is illustrated by the fact that even though the high-energy component of the discrete auroral case is five times more important than the kappa component, the resulting temperature increase is only of the order of 100 K in the 250-500 km region. This thermostatic effect stems from the temperature dependence of the IR cooling efficiency (below the homopause, from the hydrocarbons) which increases with increasing temperature. Therefore heating the homosphere produces a temperature increase which is partly balanced by the temperature decrease due to the higher hydrocarbon IR cooling efficiency.

The net heating rate integrated above the homopause is 28 ergs cm^{-2} s^{-1} for the discrete auroral case and 25 ergs cm^{-2} s^{-1} for the diffuse auroral case. These heating rate excesses are sufficient to sustain exospheric temperature of the order of 1300 K, and H_2 and H_3^+ temperatures within the observational range. Below the homopause, the heating processes that we consider and the downward heat conduction cannot balance the efficient hydrocarbon cooling. A critical pressure of 1 μbar is therefore imposed (horizontal bar in Figure 5) which defines the level below which unspecified heat sources will prevent the thermal profile from cooling down.

6.5. UV and IR Emissions

6.5.1. Diffuse auroral case. We examine the total H_2 emission, the associated color ratio and the IR emissions.

6.5.1.1. H_2-FUV emission: The kappa energy distribution of the diffuse auroral case is constrained by the multiple fits to the EPD energetic electron distribution measured by Galileo between 10 and 20 R_J. The energy flux contained in this kappa component is set to 20 ergs cm^{-2} s^{-1} by the observational constraints. Since the high-energy cutoff of this distribution is not higly constrained

Table 4. Contribution of the Different Heat Sources to the Total Heating

Heat sources	Contribution to Total	
	Diffuse	Discrete
Chemical heating	68.4 %	68.1 %
Vibrations + rotations	15.5 %	15.7 %
H_2 dissociation from singly excited states	7.0 %	7.1 %
Lyman and Werner bands heating	5.9 %	6.0 %
Electron heating	2.4 %	2.4 %
H_2 dissociation from doubly excited states	0.8 %	0.75 %

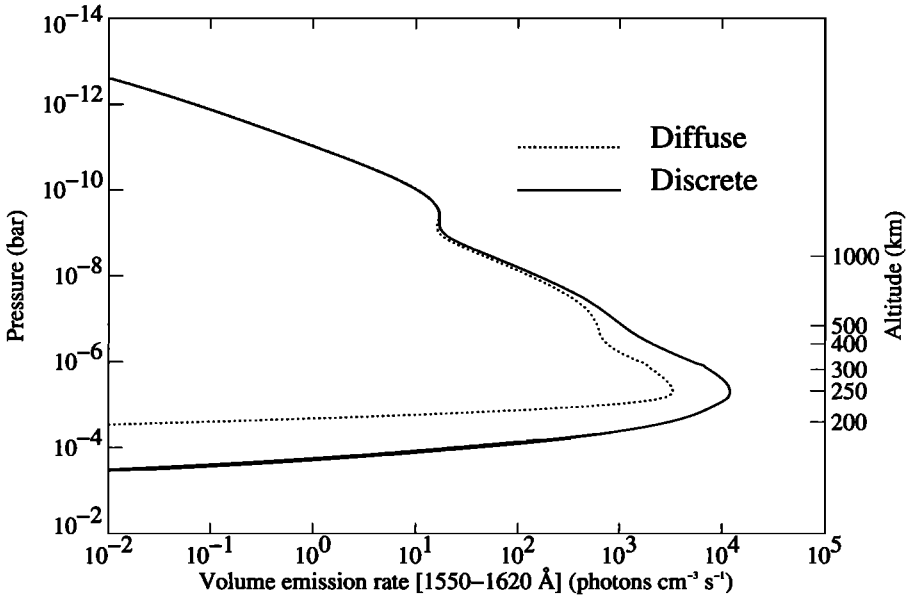

Figure 6. Vertical H_2-FUV volume emission rate profile in the 1550-1620 Å wavelength range calculated with the spectral generator [*Dols et al.*, 2000] for the discrete (solid line) and diffuse (dashed line) energy distributions. The altitude axis refers to the discrete auroral case.

by the observation, we consider it as a free parameter. By setting it to 85 -keV it was possible to force the kappa distribution to give rise to an H_2-FUV emission peaking at 245 km, in agreement with the Galileo visible emission peak (245 ±30 km) although this observed altitude corresponds to a discrete emission measured close to the limb.

The energy flux carried by the 100-eV and 3-keV soft electron components has been set to 0.5 and 10 ergs cm^{-2} s^{-1}, respectively, to meet the observational constraints on the temperature profile and on the EUV emissions [*Ajello et al.*, submitted, 2000]. This energy distribution gives rise to a vertical unattenuated total H_2-FUV emission (900-1700 Å) of 295 kR, in agreement with the typical brightness of 300 kR deduced from the observations. The corresponding volume emission rate profile in the 1550-1620 Å wavelength range is plotted in Figure 6. The most striking feature is the humped shape of the emission profile, similar to the shape of the heating rate and ion production rates vertical profiles. The upper hump peaks at an altitude of 1300 km, controlled by the characteristic energy of the 100-eV soft electron Maxwellian distribution. The central hump is not pronounced; an inflection point is located around 600 km and is controlled by the characteristic energy of the 3-keV soft component. The lower emission peak is controlled by the energy cutoff and by the characteristic energy of the kappa distribution and peaks at an altitude of 245 km. It should be noted that the upper hump has a maximum volume emission rate 3 orders of magnitude lower than that of the lower hump. Therefore its presence in a diffuse aurora would probably be impossible to detect.

In order to estimate the H_2 temperature, the H_2-FUV emission vertical profile is used to weight the temperature vertical profile. Since the lower emission peak puts the weight on a cold part of the temperature profile and the upper emission on warmer region, the relative importance of the soft and hard components has a critical influence on the H_2 temperature. It was already stated that the kappa component of the energy distribution does not produce significant heat in the homosphere that remains at an average temperature of 200 K. The corresponding H_2-FUV emission therefore contributes to a low H_2 temperature of the order of 200 K. On the other hand, the soft electron components are responsible for the high temperatures reached in the heterosphere and their resulting UV emission increases the H_2 temperature to 473 K, a value within the observational range (400-800 K).

6.5.1.2. Color ratio: The C color ratio represents the ratio between the unabsorbed and absorbed FUV emissions and therefore is a signature of the amount of emission produced below the level of methane absorption unit optical depth $(\tau_{CH4}=1)$ at ~250 km. It is controlled by the energy distribution of the hard component (that is the characteristic energy and high-energy cutoff of the kappa distribution) and by the relative importance of the soft and hard component energy fluxes.

The kappa component gives rise to an H_2-FUV emission peaking close to the $(\tau_{CH4}=1)$ level corresponding to a color ratio of the order of 1.5. It is significantly decreased by the presence of the upper emission due to the soft components and reaches a final value of 1.25, for a vertical emission, slightly lower than the observational constraint (1.5-3.6). This value corresponds to the attenuation by an overlying CH_4 column density of $7X10^{15}$ cm^{-2}, which is also below the observational range. For an observation at 60° zenith angle the color ratio slightly increases to 1.34 corresponding to a CH_4 column density of $1.1\ X10^{16}$ cm^{-2}.

This first case illustrates the difficulty to get both the H_2 temperature and the color ratio in the observational ranges. In order to increase the color ratio one would increase the FUV emission below the homopause, however, by doing so the weight on the vertical thermal profile would be shifted downward in a colder region resulting in a lower H_2 temperature. A trade-off is therefore necessary between the color ratio and the H_2 temperature, which is almost reached for an FUV emission peaking at 245 km.

6.5.1.3. IR emissions. The calculated vertically integrated H_3^+ thermal emission (11 ergs cm^{-2} s^{-1}) is one order of magnitude higher than the average emission observed in a diffuse aurora (1.5

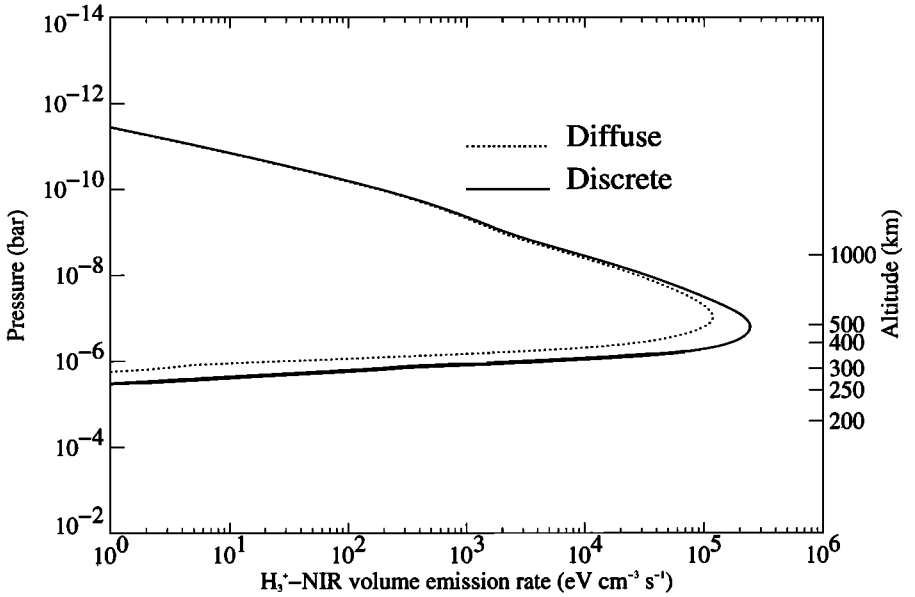

Figure 7. Vertical H_3^+-NIR volume emission rate profile for the discrete (solid line) and diffuse (dashed line) energy distributions. The altitude axis refers to the discrete auroral case.

erg cm^{-2} s^{-1}). It corresponds to an H_3^+ column of 1.8x10^{13} cm^{-2}, which is within the observational range (1.25-6.25x10^{13} cm^{-2}). The discrepancy between the H_3^+-NIR emission and the associated column density may be explained by the temperature dependence of the IR emission. Since the H_3^+ thermal IR emission is proportional to the temperature, it does not only depend on the amount of H_3^+ ions produced but also on the altitude at which they are created. Hence a large production of H_3^+ in a cold region does not necessarily lead to a high IR emission. Inversely, a faint H_3^+ production in a warm region can be responsible for an important thermal emission.

The volume emission rate profile is represented in Figure 7. Unlike the H_2-FUV emission, the H_3^+ emission profile peaks at a pressure of 10^{-7} bar which approximately corresponds to the level from which the chemical loss of H_3^+ by the hydrocarbons becomes significant. Accordingly, this level mainly depends on the altitude of the CH_4 homopause rather than on the energy of the kappa component. The destruction of H_3^+ by methane and the effect of exospheric heating on the H_3^+ emission intensity are expected to lead to skewed auroral morphologies for the H_2-UV and H_3^+ thermal emissions.

In analogy with the H_2-FUV emission the H_3^+ emission profile is used to weight the thermal profile and allows to set the H_3^+ temperature to 744 K, in the lower part of the observational range (700-1100 K).

In order to estimate the hydrocarbon IR emissions we have accounted for radiative transfer effects by assuming that the thermal IR radiation is able to leave the hydrocarbon layer above levels corresponding to a CH_4 integrated column of 5.3x10^{17} cm^{-2} and a C_2H_2-integrated column of 7x10^{15} cm^{-2}, respectively. For the diffuse auroral case these columns are reached at 211 km (1.6x10^{-5} bar) and 184 km (4.7x10^{-5} bar), respectively.

The CH_4 integrated thermal emission reaches 47 ergs cm^{-2} s^{-1}, about half the value observed with IRIS in the hot spot region (without accounting for the fill factor). The C_2H_2 integrated emission is only 14 ergs cm^{-2} s^{-1}, 6 times below the value observed by IRIS. Since these IR emissions are proportional to the temperature, the latter discrepancy with the observation may be attributed to the underestimation of the temperature in the lower part of the homosphere. Higher temperatures than those deduced from IRIS are suggested by the analysis of C_2H_4 and C_2H_6 thermal IR emissions [*Kostiuk et al.*, 1993; *Livengood et al.*, 1993]. The underestimation may also stem from the approximation made on the limit of the optically thin emission region or, as suggested by *Dols et al.* [2000), to aurorally driven chemistry likely to alter the hydrocarbon abundances.

6.5.2. Discrete auroral case.

The high-energy Maxwellian component of the discrete distribution is adjusted to match the altitude of the Galileo visible emission peak (245 ± 30 km) and an H_2-FUV total brightness of ~1.MR typically observed in auroral discrete arcs. Since this high-energy component is unable to heat the heterosphere, we added the same soft electron components as in the diffuse auroral case, so that with a total energy flux of 110.5 ergs cm^{-2} s^{-1}, a vertically integrated unabsorbed brightness of 1.1 MR of total H_2-FUV is obtained.

6.5.2.1. H_2-FUV emission. The resulting emission profile is shown in Figure 6. As expected, the sole difference with the diffuse auroral case arises in the region of the lower emission peak, around an altitude of 247 km. This region presents a maximum value of the volume emission rate three times higher than the maximum emission rate produced by the kappa distribution. Since the contribution of the upper emission to the total emission is decreased by five, its influence on the estimated H_2 temperature is also reduced. Hence the H_2 temperature is mainly controlled by the high-energy component which puts more weight on the lower (colder) part of the thermal profile and gives rise to an H_2 temperature of 407 K, colder than the H_2 temperature obtained in the diffuse auroral case, but still at the lower limit of the observational range. This surprisingly low temperature may be explained by the fact that the temperature increase in the 1 μbar region, caused by the higher energy flux of the high-energy component, partly balances the temperature decrease due to the shift of the weight on the thermal profile towards colder regions. This illustrates again the difficulty to generate a higher H_2 temperature, since increasing the temperature in the 1 μbar region

by raising the energy flux of the high-energy component also shifts the weight on the thermal profile downward and does not necessarily lead to an H_2 temperature increase but may, as in this case, decrease it.

6.5.2.2. Color ratio. Since the altitudes of the emission peaks are the same in the diffuse and discrete auroral cases, only the increased relative importance of the high-energy flux is responsible for the slight increase of the FUV color ratio (1.5). This value corresponds to the attenuation by an overlying CH_4 column density of $1.7X10^{16}$ cm^{-2}, which is also in the observed range. For an observation at 60° zenith angle the color ratio increases to 1.6 corresponding to a CH_4 column density of 2.1 $X10^{16}$ cm^{-2}. This second case confirms the necessary trade-off between color ratio and H_2 temperature since, as expected, increasing the color ratio has led to an H_2 temperature decrease.

6.5.2.3. IR emissions. The hydrocarbon IR emissions (170 ergs cm^{-2} s^{-1} for CH_4 and 23 ergs cm^{-2} s^{-1} for C_2H_2) are higher than in the diffuse auroral case but remain too small to match the discrete auroral constraints. Although the high-energy Maxwellian drives five times more energy flux than the kappa component of the diffuse auroral case and most of this energy is deposited below the methane homopause, less than 20% of the resulting hydrocarbon IR emission is produced above the optically thick layers (213 km ($1.6x10^{-5}$ bar) for methane and 185 km ($4.7x10^{-5}$ bar) for acetylene). Moreover, these emissions are proportional to the gas temperature (and to the hydrocarbon densities) which does not vary much between the two cases. The underestimation of the IR emissions may therefore be the consequence of the difficulty to get a higher stratospheric temperature. It illustrates the fact that this model probably misses an efficient heat source in the stratospheric region (around 10^{-5} bar), which is not directly reached by the auroral electron beam.

The vertically integrated H_3^+ thermal emission (23 erg cm^{-2} s^{-1}) is higher than the average emission that would be observed in a discrete aurora (7.5 erg cm^{-2} s^{-1}). It corresponds to an H_3^+ column of $2.4x10^{13}$ cm^{-2}, which is bracketed by the observational range ($1.25\text{-}6.25x10^{13}$ cm^{-2}). As shown in Figure 7, the H_3^+ thermal emission profile is dependent on the total energy flux. As expected, the increased emission, with respect to the diffuse auroral case, is due to the more important high-energy component which increases the temperature and the H_3^+ density between 300 and 500 km. As already mentioned, the altitude of the maximum only depends on the level of the homopause. It is therefore almost insensitive to the high-energy component of the energy distribution, although this component itself influences the altitude of the homopause. It should be noted that even with a high-energy component five times more important, the H_3^+-integrated emission rate only increases by a factor of 2. Accordingly, the H_3^+ thermal emission cannot be used to estimate the total auroral energy input in the Jovian atmosphere but should be seen as a proxy for the energy carried by the soft electron component. The H_3^+ temperature is exactly the same as in the discrete auroral case (744 K). This casual similarity stems from the compensation of two effects: the high-energy component increases the temperature in the 300-500 km region so that the H_3^+ temperature should be raised; however, this temperature increase is canceled by the shift of the emission downward, which moves the weight on the average temperature to a colder region.

7. Sensitivity Studies

We now consider the sensitivity of the outputs to four parameters: the characteristic energy of the high-energy component, the H_3^+ quenching rate for the translation-vibration reaction, the eddy diffusion coefficient, and the critical pressure.

7.1. Sensitivity to the Characteristic Energy of the High-Energy Component

The penetration depth of the electron beam was already investigated in the analysis of the ion production, the heating rate, and the emission rate profiles. So far we have considered that the peak of the H_2 emission is located at an altitude of 245 km, determined from the H_2 visible emission profile observed with Galileo. However, this altitude is uncertain within a range of ± 30

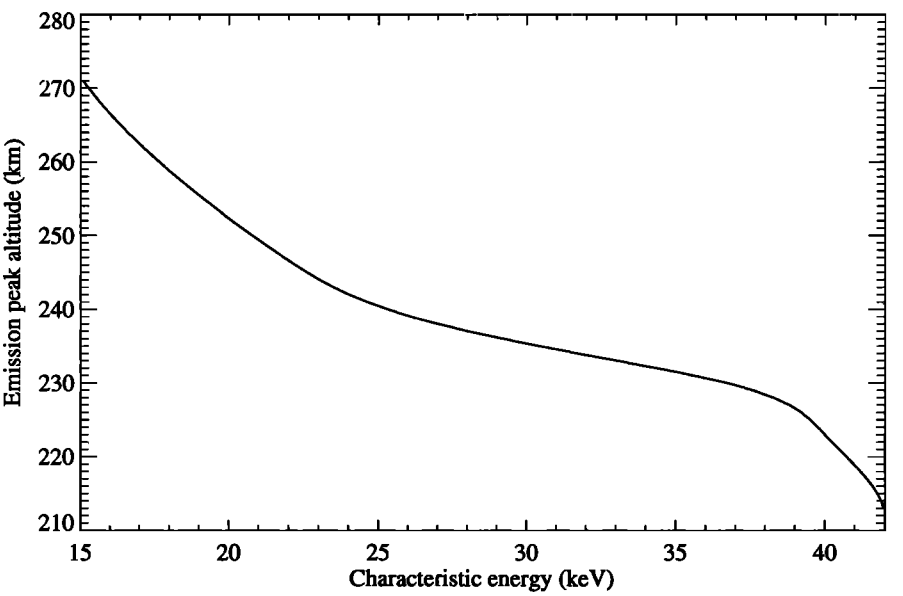

Figure 8. H_2-FUV emission peak altitude as a function of the characteristic energy of the high-energy component of the discrete auroral distribution.

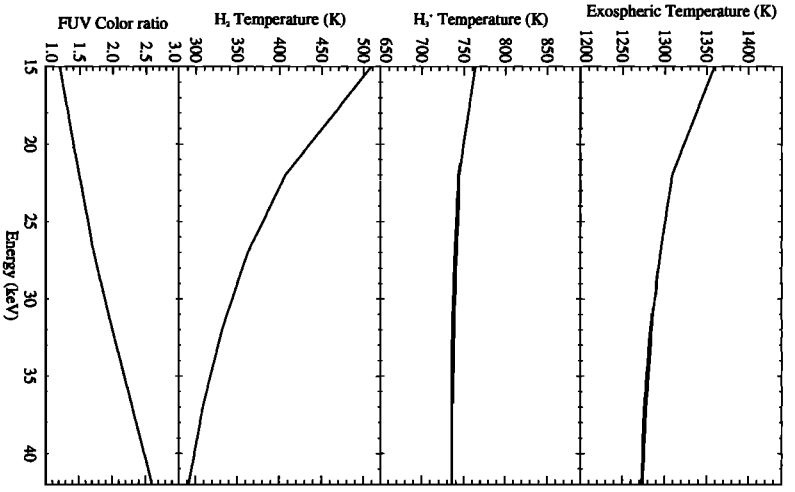

Figure 9. FUV color ratio, H_2, H_3^+, and exospheric temperatures as a function of the characteristic energy of the high-energy component of the discrete auroral distribution. The temperature axes are at the same scale for the three temperature plots.

km. W. R. Pryor et al. (Jupiter's UV aurora on Galileo Orbit G7, *Icarus*, in press, 2000) used the FUV/MUV/violet ratios on a Galileo spectrum acquired along orbit G7 to deduce a peak altitude between 275 and 295 km for a Chapman function representing the auroral excitation in the *Gladstone et al.* [1998] atmospheric model. These results suggest that an emission altitude peak of 275 km, corresponding to the upper limit set by the visible Galileo images, might be reasonable.

These altitudes may be reached by adjusting the characteristic energy of the high-energy Maxwellian component of the discrete auroral case or by adjusting the high-energy cutoff of the kappa distribution of the the diffuse auroral case.

Figure 8 shows the altitude of H_2-FUV emission peak as a function of the characteristic energy of the high-energy component of the discrete auroral case. It can be seen that an altitude of 275 km is reached with a characteristic energy of 14-keV, while the deeper emission peak at 215 km stems from a characteristic energy of 42-keV. Between these two altitudes the evolution of the emission peak altitude with energy is far from linear and a plateau is reached in the 225-250 km region. This plateau corresponds to the onset of the high-temperature gradient which gives rise to a fast H_2 scale height increase below the homopause and damps the effects due to a modification of the characteristic energy.

A similar altitude-energy curve is obtained by moving the high-energy cutoff of the kappa component of the diffuse auroral case. For this energy distribution an emission peak altitude of 275 km corresponds to a cutoff at 50-keV, while at 110-keV, the emission peak altitude drops to 215 km.

Changing the characteristic energy has strong effects on the temperature and emission profiles. Figure 9 shows the H_2, H_3^+, and exospheric temperatures as a function of the characteristic energy of the high-energy Maxwellian (discrete aurora). Varying the characteristic energy from 15 to 42-keV decreases the H_3^+ and exospheric temperatures by 30 and 90 K, respectively. The effect is more pronounced for the H_2 temperature, which is reduced by 220 K. The H_2 and H_3^+ temperature changes are mainly explained by the altitude shift of the weight on the temperature profile by the H_2 and H_3^+ emission profiles.

Figure 9 also compares these temperature variations with the response of the FUV color ratio. It clearly illustrates, as already discussed, that the H_2 temperature varies inversely with to the color ratio. Hence, for a 15-keV characteristic energy, an H_2 temperature of 500 K is reached, but it corresponds to an almost unattenuated color ratio of 1.2. Increasing the color ratio to 2.6 with a more energetic beam (42-keV) decreases the H_2 temperature to 300 K.

7.2. Sensitivity to the H_3^+ Quenching Rate Coefficient

To date, there are no direct measurements of rate coefficients of elementary processes occurring during quenching of H_3^+ by H_2 and we considered the phenomenological rate coefficient (2.7 ± 0.6)x10^{-10} cm^3 s^{-1} determined by *Kim et al.* [1974]. It is based on a simplified reaction rate that does not account for the distribution of excited states of H_3^+. Also, it is not known whether deactivation occurs directly from each vibrational state to the ground state or by sequential deactivation in a number of collisions. This quenching coefficient therefore represents only an average or overall value. In order to test the effect of a different quenching rate this parameter has been arbitrarily halved (1.35x10^{-10} cm^{-3} s^{-1}). As expected, the H_3^+ temperature increases from 744 to 810 K, and the exospheric temperature was raised from 1309 to 1558 K. Since the effect of the quenching rate is mostly confined to the region where H_3^+ is present, the H_2 temperature only slightly increases from 407 to 429 K. The H_3^+ emission drop is entirely balanced by the emission growth due to the higher temperature, accordingly the integrated H_3^+ brightness remained at 23 ergs cm^{-2} s^{-1}. The other outputs (altitude of the emission peak, color ratio, etc.) are practically unaffected by halving the quenching rate.

The cooling effect of H_3^+ can be further examined with an extreme case where the quenching rate is set to 0, that is, where H_3^+ cooling is ignored. In such a situation the exospheric temperature reaches an exotic value greater than 17000 K. The H_3^+ temperature is around 4800 K, and the H_2 temperature reaches 2700 K. Surprisingly, the other outputs (color ratio, etc.) do not vary much. This case clearly illustrates the thermostatic role of H_3^+, which prevents the atmosphere from blowing away, even with a moderate auroral energy flux.

7.3. Sensitivity to the Eddy Coefficient Coefficient

The eddy coefficient at the homopause (K_H) plays a key role in the control of the methane density profile, especially in the region

of the H_2 emission peak as it defines the altitude of the homopause. The discrete auroral case has been tested with an eddy coefficient K_H set to 1.4×10^7 cm^2 s^{-1} that is 1 order of magnitude higher than in the initial discrete auroral case. This leads to an homopause altitude of 386 km, 66 km higher than previously. The corresponding higher CH_4 density is responsible for the drop (25 %) of the H_2 temperature as CH_4 cools down the region where most of the auroral energy is converted into heat. As a result of the smaller H_3^+ column, which is destroyed by the additional CH_4 molecules, the H_3^+ temperature increases by 42 K. The decrease of the H_3^+ column also implies a decrease of the H_3^+ IR emission by a factor of 3. The vertically integrated CH_4 column above the H_2 emission peak (4.1×10^{16} cm^{-2}) and the FUV color ratio (2.3) are almost twice as large as the initial values. Upwelling of methane due to the large amount of auroral energy deposited near the homopause may indeed cause redistribution of the CH_4 mixing ratio above the homopause similar to the O_2/N enrichment observed in the Earth auroral thermosphere. In such a case, additional heat should be available to account for a sufficiently high H_2 temperature.

7.4. Sensitivity to the Critical Pressure

The critical pressure is the pressure level below which only net heating is allowed, it represents the potential effect of unspecified heat sources possibly located below this level. We have tested the effect of increasing this pressure to 10^{-5} bar in the discrete auroral case. The major consequence is a decrease of the temperature gradient in the homopause region, which in turn reduces the H_2 temperature by 35 K. On the other hand, the H_3^+ and exospheric temperatures are little affected by this modification. This illustrates the weak thermal coupling between the upper and lower parts of the atmosphere. The methane thermal IR emission is significantly sensitive to the temperature in the homopause region. Hence, reducing the temperature by ~30 K in the 1 μbar region produces a 50% drop of the integrated CH_4-NIR emission rate. The same test was performed on the diffuse auroral case and led to similar results.

8. Conclusion

A one-dimensional model has been developed that couples a two-stream electron transport model of energy deposition with a 1-D thermal conduction model including particle heating, CH_4, C_2H_2, and H_3^+ cooling. The initial atmospheric structure is defined by a thermal profile deduced from Galileo observations. The code allows to monitor the energy degradation of an electron beam as it penetrates into this atmosphere which self-consistently adapts to the auroral conditions. The resulting thermal profile, UV and IR emissions profiles, FUV color ratio, and densities generated by various choices of the precipitating electron energy distribution are constrained by data derived from spectra and images taken in different spectral bandpasses.

Two energy distributions have been considered to simulate the effects of a diffuse aurora, usually observed in the polar cap and afternoon sectors of the auroral region, and of a discrete aurora generally observed in the morning sector of the northern auroral region. The high-energy component of the diffuse auroral energy distribution is derived by fitting measured Galileo EPD near-isotropic distributions with a kappa function. Its high-energy cutoff is set to 85-keV in order to produce an H_2-FUV emission peaking at 245-km. Likewise, the characteristic energy of the high-energy Maxwellian component of the discrete distribution is set to 22-keV to meet the 245 km constraint. In both cases, two soft electron Maxwellian components (at 100-eV and 3-keV) are added in order to meet the temperature constraints in the heterosphere.

It is shown that the 22-keV component and the kappa component heat a region of the homosphere between 10^{-4} and 10^{-6} bar and have a considerable effectiveness on the H_2 temperature. The 3-keV component heats the region directly above the homopause, between 10^{-6} and 10^{-9} bar and has the largest influence on the H_2 and H_3^+ temperatures. The 100-eV component is responsible for the net heating in the thermosphere, from 10^{-9} to 10^{-12} bar and exerts a control on the exospheric temperature.

Comparison of the calculated diffuse and discrete H_3^+ thermal emissions indicates that this emission is principally sensitive to the level of soft electron component and responds only moderately to the high-energy component. Therefore the H_3^+ thermal emission cannot be used to estimate the total auroral energy input in the Jovian atmosphere but should be seen as a proxy for the energy contained in the soft electron component.

The temperature dependence of the hydrocarbon thermal IR cooling efficiency is partly responsible for preventing the high-energy component to give rise to a substantial temperature increase in the homosphere. The underestimation of these hydrocarbon IR emissions by the model supports the idea that it probably misses an efficient heat source in the stratospheric region, which is not directly reached by the auroral electron precipitation. The need in this model of a critical pressure below which cooling is inefficient confirms that the auroral energy precipitated and the heat conducted downward are not enough to balance the hydrocarbon cooling below the homopause. Nonparticle heating, such as Joule heating or breaking gravity waves, and indirect auroral processes, like exothermic hydrocarbon chemistry, need to be specified as well.

Sensitivity tests were performed to evaluate the importance of the energy spectrum of the incident electrons for the thermal balance of Jupiter's auroral thermosphere. They show that the FUV color ratio increases with the characteristic energy of the high-energy component while the H_2 rovibrational temperature varies inversely with the energy. A trade-off is therefore necessary for these two parameters to simultaneously meet the observational constraints. A sufficiently high H_2 temperature may be simulated by shifting the H_2 emission profile toward higher altitudes. However, this shift places most of the H_2 emission above the methane homopause, which reduces the FUV color ratio and the hydrocarbon IR emissions to unobserved values. This result is in agreement with calculations performed with monoenergetic beams [*Perry et al.*, 1999] which show that the temperatures near the altitude of peak energy deposition are significantly lower than those derived from rotational analyses of auroral H_2 emissions.

It is shown that halving the H_3^+ quenching rate leads to higher exospheric and H_3^+ temperatures and leaves the H_2 temperature almost unchanged. Setting the quenching rate to 0 allows us to illustrate the essential thermostatic role played by H_3^+, which regulates the heating in the thermosphere and thus the atmospheric expansion. An increased eddy diffusion reproduces the effect of a possible auroral upwelling of methane, especially, it increases the color ratio, but gives rise to an H_2 temperature smaller than the observed value.

It has been stressed that the multispectral observational constraints have been established from measurements that are not simultaneous in time and space. Moreover, since these observations probe different altitude regions of the atmosphere,

they do not necessarily stem from the same processes. A campaign of simultaneous multispectral observations of Jupiter's aurora would allow a more reliable determination of the complete energy budget of the precipitating electrons and would give some clues on the possible link between the different auroral signatures.

Acknowledgments. We would like to thank Vincent Dols for providing us with his H_2 spectral generator code, Randy Gladstone and Tariq Majeed for their help. Support for this work was provided by the PRODEX ESA program funded by the Belgian Federal Office for Scientific, Technical and Cultural Affairs - Prime Minister's Services. J.C.G. is supported by the Belgian Foundation for Scientific Research (FNRS).

Michel Blanc thanks Timothy Livengood and another referee for their assistance in evaluating this paper.

References

Abgrall, H., E. Roueff, X. Liu, and D.E. Shemansky, The emission continuum of electron excited molecular hydrogen, *Astrophys. J., 481*, 557, 1997.

Abgrall, H., E. Roueff, X. Liu, D.E. Shemansky, and G.K. James, High-resolution far ultraviolet emission spectra of electron-excited molecular deuterium, *J. Phys. B. At. Mol. Opt. Phys., 32*, 3813, 1999.

Ajello, J.M., and D.E. Shemansky, Electron excitation of the $H_2(a\ ^3\Sigma_g^+ \rightarrow b\ ^3\Sigma_u^+)$ continuum in the vacuum ultraviolet, *Astrophys. J., 407*, 820, 1993.

Ajello, J.M., D. Shemansky, T.L. Kwok, and Y.L. Yung, Studies of extreme-ultraviolet emission from Rydberg series of H_2 by electron impact, *Phys. Rev. A, 29*, 636, 1984.

Ajello, J.M., D.E Shemansky, and G.K. James, Cross sections for production of H(2p, 2s, 1s) by electron collisional dissociation of H_2, *Astrophys. J., 371*, 422, 1991.

Ajello, J.M., I. Kanik, and S.M. Ahmed, Line profile of H Lyman α from dissociative excitation of H_2 with application to Jupiter, *J. Geophys. Res., 100*, 26,411, 1995.

Ajello, J.M., S.M. Ahmed and X. Liu, Line profile of H Lyman β from dissociative excitation of H_2, *Phys. Rev., 53*, 2302, 1996.

Auerbach, D., R. Cacak, R. Candano, T.D. Gaily, C.J. Keyser, J.W. McGowan, J.B.A. Mitchell, S.F.J. Wilk, Merged electron-ion beam experiments, I, Methods and measurements of $(e\text{-}H_2^+)$ and $(e\text{-}\ H_3^+)$ dissociative recombination cross sections, *J. Phys. B, 10*, 3797, 1977.

Bandyopadhyay, A., K. Roy, P. Mandal, and N.C. Sil, Single-differential total ionization cross sections of hydrogen atom by electron impact, *Phys. Rev. A, 51*, 2151, 1995.

Banks, P.M., and G. Kockarts, *Aeronomy, Part B*, Academic, San Diego, Calif., 1973.

Banks, P.M., and A.F. Nagy, Concerning the influence of elastic scattering upon photoelectron transport and escape, *J. Geophys. Res., 75*, 1902, 1970.

Bhattacharya, B., R.M. Thorne, S.J. Bolton, D.J. Williams, and D. Gurnett, Recirculating Magnetospheric Electrons as a Source for the Jovian Aurora, *Eos Trans. AGU, 79*, Fall Meet. Suppl., F549, 1998.

Broadfoot, A.L., M.J.S. Belton, P.Z. Takacs, B.R. Sandel, D.E. Shemansky,J.B. Holberg, J.M. Ajello, S.K. Atreya, T.M. Donahue, H.W. Moos, J.L.Bertaux, J.E. Blamont, D.F. Strobel, J.C. McConnell, A. Dalgarno, R. Goody and M.B. McElroy, Extreme ultraviolet observations from Voyager 1 encounter with Jupiter, *Science 204*, 979, 1979.

Buckman, J.B., M.J. Brunger, D.S. Newman, G. Snitchler, S. Alston, D.W. Norcross, M.A. Morrison, B.C. Saha, G. Dandy, and W.K. Trail, Near-threshold vibrational excitation of H_2 by electron impact : resolution of discrepancies between experiment and theory, *Phys. Rev. Lett.,65* , 3253, 1990.

Caldwell, J., A.T. Tokunaga, and F.C. Gillett, Possible infrared aurorae on Jupiter, *Icarus*, *44*, 667, 1980.

Callaway, J., and K. Unnikrishnan, Electron impact excitation of the n=3 and n=2 states of hydrogen atom at intermediate (14-100 eV) energies, *Phys. Rev. A, 48*, 4292, 1993.

Clarke, J.T., L. Ben Jaffel, A. Vidal-Madjar, G.R. Gladstone, J.H. Waite Jr., R. Prangé, J.-C. Gérard, J. Ajello, and G. James, Hubble Space Telescope Goddard High-Resolution Spectrograph H_2 rotational spectra of Jupiter's aurora, *Astrophys. J., 430*, L73, 1994.

Clarke, J.T., G. Ballester, J. Trauger, J Ajello, W. Pryor, K. Tobiska, J.EP. Connerney, G.R. Gladstone, J.H. Waite Jr., L. Ben Jaffel, and J.-C. Gérard, Hubble Space Telescope imaging of Jupiter's UV aurora during the Galileo orbiter mission, *J. Geophys. Res., 103*, 20,217, 1998.

Dabrowsky, I., The Lyman and Werner bands of H_2, *Can. J. Phys., 62*, 1639, 1984.

Dalgarno, A., and T.L. Stephens, Discrete absorption and photodissociation of molecular hydrogen, *Astrophys. J., 160*, L107, 1970.

Datz, S., G. Sundström, Ch. Biedermann, L. Brodström, H. Danared, S. Mannervik, J.R. Mowar, and L. Larsson, Branching processes in the dissociative recombination of H_3^+, *Phys. Rev. Lett., 74*, 896, 1995.

Dols, V., J.-C. Gérard, J.T. Clarke, J. Gustin, and D. Grodent, Diagnostics of the Jovian aurora deduced from ultraviolet spectroscopy: Model and GHRS observations, *Icarus, 147*, 251, 2000.

Dougherty, M. K., D. J. Southwood, A. Balogh and E. J. Smith, Field Aligned Currents in the Jovian Magnetosphere During the Ulysses Flyby, *Planet. Space Sci., 41*, 291, 1993.

Drossart, P., J.-P. Maillard, J. Caldwell, S.J. Kim, J.K.G. Watson, W.A. Majewski, J. Tennyson, S. Miller, S.K. Atreya, J.T. Clarke, J.H. Waite Jr., and R. Wagener, Detection of H_3^+ on Jupiter, *Nature, 340,* 539, 1989.

Drossart, P., B. Bézard, S.K. Atreya, J. Bishop, J.H. Waite, and D. Boice, Thermal profiles in the auroral regions of Jupiter, *J. Geophys. Res., 98*, 18,803, 1993a.

Drossart, P., J-.P. Maillard, J. Caldwell, and J Rosenqvist, Line-resolved spectroscopy of the Jovian H_3^+ auroral emission at 3.5 micrometers, *Astrophys. J., 402*, L25, 1993b.

Garvey , R.H., H.S. Porter, and A.E.S. Green, Relativistic yield spectra for H_2, *J. Appl. Phys., 48*, 4353, 1977.

Gérard, J.-C., and V. Singh, A model of energetic electrons and EUV emission in the Jovian and Saturnian Atmospheres and implications, *J. Geophys. Res., 87*, 4525, 1982.

Gérard, J.-C., V. Dols, F. Paresce, and R. Prangé, Morphology and time variation of the Jovian far UV aurora: Hubble Space Telescope observations, *J. Geophys. Res., 98*, 18,793, 1993.

Gérard, J.-C., D. Grodent, R. Prangé, J.H. Waite Jr.,G.R. Gladstone, V. Dols, F. Paresce, A. Storrs, L. Ben Jaffel, and K.A. Franke, A remarkable auroral event on Jupiter observed in the ultaviolet with the Hubble Space Telescope, *Science, 266*, 1675, 1994.

Gérard, J.-C., D. Grodent, V. Dols, and J.H. Waite Jr., The longitudinal variation of the color ratio of the Jovian ultraviolet aurora: A geometric effect?, *Geophys. Res. Lett., 25*, 1601, 1998.

Gladstone, G.R., Radiative transfer and photochemistry in the upper atmosphere of Jupiter, Ph.D. thesis, Calif. Inst. of Technol., Pasadena, 1982.

Gladstone, G.R., M. Allen, and Y.L. Yung, Hydrocarbon photochemistry in the upper atmosphere of Jupiter, *Icarus, 119*, 1, 1996.

Gladstone, G.R., J.H. Waite Jr., J.-C. Gérard, Jovian auroral Ly-α self-reversals: A window on Jupiter's auroral electrojet? , *Bull. Am. Astron. Soc., 30*, 1078, 1998.

Glass-Maujean, M, Transition probabilities for the D and B' vibrational levels to the X vibrational levels and continuum of H_2, *Atomic Data Nucl. Data Tables, 30*, 301, 1984.

Green, A. E. S., and T. Sawada, Ionization cross sections and secondary electron distributions, *J. Atmos.Terr. Phys., 34*, 1719, 1972.

Grodent, D., G.R. Gladstone, J.-C. Gérard, V. Dols, and J.H. Waite Jr., Simulation of the morphology of the Jovian UV north aurora observed with the Hubble Space Telescope, *Icarus, 128*, 306, 1997.

Grodent, D., Modeling of the auroral thermal structure and morphology of Jupiter, Ph.D. thesis, Univ. de Liège, Liège, Belgium, 2000.

Ham, D.O., D.W. Trainor, and F. Kaufman, Gas phase kinetics of H + H + $H_2 \rightarrow 2H_2$, *J. Chem. Phys., 53*, 4395, 1970.

Hanley, H.J.M., R.D. McCarty, and H. Inteman, The viscosity and thermal conductivity of dilute gaseous hydrogen from 15 to 5000 K, *J. Res. Natl. Bur. Stand., 74A*, 331, 1970.

Harris, W., J.T. Clarke, M.A. McGrath and G.E. Ballester, Analysis of Jovian auroral H Ly-α emission (1981-1991), *Icarus, 124*, 350, 1996.

Heaps, M.G., J.N. Bass, and A.E.S. Green, Electron excitation of a Jovian aurora, *Icarus, 20*, 297, 1973.

Horanyi, M., T.E. Cravens, and J.H. Waite Jr., The precipitaion of energetic heavy ions into the upper atmosphere of Jupiter, *J. Geophys. Res., 93*, 7251, 1988.

Hunten, D.M., and A.J. Dessler, Soft electrons as a possible heat source for Jupiter's thermosphere, *Planet. Space Sci., 25*, 817, 1977.

Ingersoll, A.P., A.R. Vasavada, B. Little, C.D. Anger, S.J. Bolton, C. Alexander, K.P. Klaasen, W.K. Tobiska, Imaging Jupiter's aurora at visible wavelengths, *Icarus, 135*, 251, 1998.

Jackman, C.H., R.H. Garvey, and A.E.S. Green, Electron impact on atmospheric gases, a, Updated cross sections, *J. Geophys. Res., 82*, 5081, 1977.

James, G.K., J.A. Slevin, D.E. Shemansky, J.W. McConkey, I. Bray, D. Dziczek, I. Kanik, and J.M. Ajello, Optical excitation function of H(1*s*-2*p*) produced by electron impact from threshold to 1.8-keV , *Phys. Rev. A, 55*, 1069, 1997.

James, G.K., J.M. Ajello, and W.R. Pryor, The middle ultraviolet visible spectrum of H_2 excited by electron impact, *J. Geophys. Res., 103*, 20,113, 1998

Khakoo, M.A., and J. Segura, Differential cross sections for the electron impact excitation of the b $^3\Sigma_u^+$ continuum of molecular hydrogen, *J. Phys. B, 27*, 2355, 1994.

Khakoo, M.A., and S. Trajmar, Electron-impact of the a $^3\Sigma_g^+$, B $^1\Sigma_u^+$, b $^3\Sigma_u^+$ and C $^1\Pi_u$ states of H_2, *Phys. Rev. A, 34*, 146, 1986.

Kim, J.K., L.P. Theard, and W.T. Huntress Jr., Reactions of excited and ground state H_3^+ ions with simple hydrides and hydrocarbons: Collisional deactivation of vibrationally excited H_3^+ ions, *Int. J. Mass Spectrom. Ion Phys., 15*, 223, 1974.

Kim, Y.H., J.L. Fox, and H.S. Porter, Densities and vibrational distribution of H_3^+ in the Jovian auroral ionosphere, *J. Geophys. Res., 97*, 6093, 1992.

Kim, Y.H., J.L. Fox, and J.J. Caldwell, Temperatures and altitudes of Jupiter's ultraviolet aurora inferred from GHRS observations with the Hubble Space Telescope, *Icarus, 128*, 189, 1997.

Kostiuk, T., R. Romani, F.Espenak, T.A. Livengood, and J.J. Goldstein, Temperature and abundances in the Jovian auroral stratosphere, 2, Ethylene as a probe of the microbar region, *J. Geophys. Res., 98,* 18823, 1993.

Kwok, T.L., A. Dalgarno, and A. Posen, Transition probabilities of the (B' $\Sigma_u^+ \rightarrow X\ ^1\Sigma_g^+$) system of molecular hydrogen, *Phys. Rev. A, 32*, 646, 1985.

Lam, H.A., N. Achilleos, S. Miller, J. Tennyson, L.M. Trafton, T.R. Geballe, and G.E. Ballester, A baseline spectroscopic study of the infrared auroras of Jupiter, *Icarus, 127*, 379, 1997.

Linder, F., and H. Schmidt, Rotational and vibrational excitation of H_2 by slow electron impact, *Z. Naturforsch., 260*, 10, 1971.

Liu, W., and A. Dalgarno, The ultraviolet spectrum of the Jovian aurora, *Astrophys. J., 467*, 446, 1996.

Liu, W., and D.R. Shultz, Ultraviolet emission from oxygen precipitating into jovian aurora, *Astrophys. J., 530*, 500, 2000.

Liu, X., S.M. Ahmed, R.A. Multari, G.K. James, and J.M. Ajello, High-resolution electron-impact study of far-ultraviolet emission spectrum of molecular hydrogen, *Astrophys. J. Suppl., 101*, 375, 1995.

Liu, X., D.E. Shemansky, S.M. Ahmed, G.K. James, and J.M. Ajello, Electron-impact excitation and emission cross sections of the H_2 Lyman and Werner systems, *J. Geophys. Res., 103*, 26,739, 1998.

Livengood, T.A., D.F. Strobel, and H.W. Moos, Long-term study of longitudinal dependence in primary particle precipitation in the north Jovian aurora, *J. Geophys. Res., 95*, 10,375, 1990.

Livengood, T.A., T. Kostiuk, F. Espenak, and J.J. Goldstein, Temperature and abundances in the Jovian auroral stratosphere, 1. Ethane as a probe of the millibar region, *J. Geophys. Res., 98*, 18,813, 1993.

Maillard, J.P., P. Drossart, J.K.G. Watson, J. J. Kim, and J. Caldwell, H_3^+ fundamental band in Jupiter's auroral zones at high resolution from 2400 to 2900 inverse centimeters, *Astrophys. J., 363*, L37, 1990.

Matcheva, K.I., and D.F. Strobel, Heating of Jupiter's thermosphere by dissipation of gravity waves due to molecular viscosity and heat conduction, *Icarus,* 140, 328, 1999.

Miles, W.T., R. Thompson, and A.E.S. Green, Electron impact cross sections and energy deposition in molecular hydrogen, *J. Appl. Phys., 43*, 678, 1972.

Miller, S., R.D. Joseph, and J. Tennyson, Infrared emissions of H_3^+ in the atmosphere of Jupiter in the 2.1 and 4.0 micron region, *Astrophys. J., 360*, L55, 1990.

Moiseiwitsch, B.L., Elastic scattering of electrons, *Atmos. Mol. Process,* 280, 1962.

Morrissey, P.F., P.D. Feldman, J.T. Clarke, B.C. Wolven, D.F. Strobel, S.T. Durrance, and J.T. Trauger, Simultaneous spectroscopy and imaging of the Jovian aurora with the Hopkins Ultraviolet Telescope and the Hubble Space Telescope, *Astrophys. J., 476*, 918, 1997.

Mount, G.H., and H.W. Moos, Photoabsorption cross sections of methane and ethane, *Astroph. J., 224*, L35, 1978.

Nagy, A.F., and P.M. Banks, Photoelectron fluxes in the ionosphere, *J. Geophys. Res., 75*, 6260, 1970.

Neale, L., and J. Tennyson, A high-temperature partition function for H_3^+, *Astrophys. J., 454*, L169, 1995.

Perry, J.J., Y.H. Kim, J.L. Fox, and H.S. Porter, Chemistry of the Jovian auroral atmosphere, *J. Geophys. Res., 104*, 16,541, 1999.

Pryor, W.R., et al., Jupiter's UV aurora on Galileo orbit G7, *Icarus*, in press, 2000.

Rego, D., R. Prangé, and J.-C. Gérard, Auroral Lyman alpha and H_2 bands from the giant planets, I, Excitation by proton precipitation in the Jovian atmosphere, *J. Geophys. Res., 99*, 17,075, 1994.

Rego, D., N. Achilleos, T. Stallard, S. Miller, R. Prangé, M. Dougherty, and R.D. Joseph, Supersonic winds in Jupiter's aurorae, *Nature, 399*, 121, 1999.

Rescigno, T.N, B.K. Elza, and B.H. Lengsfield III, An ab initio treatment of near-threshold vibrational excitation of H_2 by electron impact: New perspectives on discrepancies between crossed-beam and swarn data, *J. Phys. B, 26*, L567, 1993.

Satoh, T., J.E.P. Connerney, and R.L. Baron, Emission source model of Jupiter's H_3^+ aurorae: A generalized inverse analysis of images, *Icarus, 122*, 1, 1996.

Seiff, A., D.B. Kirk, T.C.D. Knight, R.E. Young, J.D. Mihalov, L.A. Young, F.S. Milos, G. Schubert, R.C. Blanchard, and D. Atkinson, Thermal structure of Jupiter's atmosphere near the edge of a 5-μm hot spot in the north equatorial belt, *J. Geophys. Res., 103*, 22,857, 1998.

Shemansky D.E., J.M. Ajello, and D.T. Hall, Electron impact excitation of H_2: Rydberg band systems and the benchmark dissociative cross section for H Lyman-alpha, *Astrophys. J., 296*, 765, 1985.

Shyn, T.W., and W.E. Sharp, Double differential cross sections of secondary electrons ejected from gases by electron impact: 25-250 eV on H_2 (abstract), *Eos. Trans. AGU, 61*, 285, 1980.

Shyn, T.W., and W.E. Sharp, Angular distribution of electrons elastically scattered from H_2, *Phys. Rev. A, 24*, 1734, 1981.

Sommeria, J., L. Ben Jaffel, and R. Prangé, On the existence of supersonic jets in the upper atmosphere of Jupiter, *Icarus, 119*, 2, 1995.

Stephan, K., H. Helm, and T.D. Märk, Mass spectrometric determination of partial electron impact ionization cross sections of He, Ne, Ar and Kr from threshold up to 180 eV, *J. Chem. Phys., 73*, 3763, 1980.

Stephens, T.L., and A. Dalgarno, Spontaneous radiative dissociation in molecular hydrogen, *J. Quant. Spectrosc. Radiat. Transf., 12*, 569, 1972.

Stephens, T.L., and A. Dalgarno, Kinetic energy in the spontaneous radiative dissociation of molecular hydrogen, *Astrophys. J., 186*, 165, 1973.

Straub, H.C., P. Renault, B.G. Lindsay, K.A. Smith, and R.F. Stebbings, Absolute partial cross sections for electron-impact ionization of H_2, N_2,and O_2 from threshold to 1000 eV, *Phys. Rev. A, 54*, 2146, 1996.

Sundström, G., et al., Destruction rate of H_3^+ by low-energy electrons measured in a storage-ring experiment, *Science, 263*, 785, 1994.

Swartz, W.E., J.S. Nisbet, and A.E.S. Green, Analytic expression for the energy transfer rate from photoelectrons to thermal electrons, *J. Geophys. Res., 76*, 8425, 1971.

Theard, L.P., and W. T. Huntress Jr., Ion molecule reactions and vibrational deactivation of H_3^+ ions in mixtures of hydrogen and helium, *J. Chem. Phys., 60*, 2840, 1974.

Trafton, L.M., J.D.F. Lester, and K.L. Thompson, Unidentified emission lines in Jupiter's northern and southern 2 micron aurorae, *Astrophys. J., 343*, L73, 1989.

Trafton, L.M., J.C. Gérard, G. Munhoven, J.H. Waite Jr., High-resolution spectra of Jupiter's northern auroral ultraviolet emission with the Hubble Space Telescope, *Astrophys. J., 421*, 816, 1994.

Trafton, L.M., V. Dols, J.-C. Gérard, J.H. Waite, Jr., G.R. Gladstone, G. Munhoven, HST spectra of the Jovian ultraviolet aurora: Search for heavy ion precipitation, *Astrophys. J., 507*, 955, 1998.

Vasavada, A.R., A.H. Bouchez, A.P. Ingersoll, B. Little, C. D. Anger, and the Galileo SSI Team, Jupiter's visible aurora and Io footprint, *J. Geophys. Res., 104*, 27,133,142, 1999.

von Zahn, U., D.M. Hunten, and G. Lehmacher, Helium in Jupiter's atmosphere: Results from the Galieo probe Helium Interferometer Experiment, *J. Geophys. Res., 103*, 22,815, 1998.

Waite, J.H., Jr., T.E. Cravens, J.U. Kozyra, A.F. Nagy, S.K. Atreya, and R.H. Chen, Electron precipitation and related aeronomy of the Jovian thermosphere and ionosphere, *J. Geophys. Res., 88*, 6143, 1983.

Waite, J.H., Jr., F. Bagenal, F. Seward, C. Na, G.R. Gladstone, T.E. Cravens, K.C. Hurley, J.T. Clarke, R. Elsner, and S.A. Stern, ROSAT observations of the Jupiter aurora, *J. Geophys. Res., 99*, 14,799, 1994.

Waite, J.H., Jr., G.R. Gladstone, W.S. Lewis, P. Drossart, T.E. Cravens,

A.N. Maurellis, B.H. Mauk, and S. Miller, Equatorial X-ray emissions: Implications for Jupiter's high exospheric temperatures, *Science, 276*, 104, 1997.

Williams, D.J., and R.W. McEntire, The Galileo energetic particles detector, *Space Sci. Rev., 60*, 385, 1992.

Wolven, B.C., and P. Feldman, Self-absorption by vibrationally excited H_2 in the Astro-2 Hopkins Ultraviolet Telescope spectrum of the Jovian aurora, *Geophys. Res. Lett., 25*, 1537, 1998.

Young, L.A., R.V. Yelle, R.E. Young, A. Seiff, and D.B. Kirk, Gravity waves in Jupiter's thermosphere, *Science, 276*, 108, 1997.

Yung, Y.L., G.R. Gladstone, K.M. Chang, J.M. Ajello, and S.K. Srivastava, H_2 fluorescence spectrum from 1200 to 1700 by electron impact: Laboratory study and application to Jovian aurora, *Astrophys. J., 254*, L65, 1982.

J.-C. Gérard and D. Grodent, Laboratoire de Physique Atmosphérique et Planétaire, Institut d'Astrophysique et de Géophysique, Université de Liège, Avenue de Cointe 5, B-4000 Liège, Belgium. (gerard@astro.ulg.ac.be; grodent@astro.ulg.ac.be).

J. H. Waite Jr., Southwest Research Institute, 6220 Culebra Road, San Antonio, TX 78228-0510. (hunter@kronos.space.swri.edu).

(Received August 27, 1999; revised June 30, 2000; accepted August 25, 2000.)